CHARACTERIZATION OF GRAPHENE NANO PLATELETS REINFORCED WELLBORE CEMENT

By

CODY MASSION

Bachelor of Science in Mechanical Engineering

Oklahoma State University

Stillwater, OK

December 2019

Submitted to the Faculty of the
Graduate College of the
Oklahoma State University
in partial fulfillment of
the requirements for
the Degree of
MASTER OF SCIENCE
December, 2021

CHARACTERIZATION OF GRAPHENE NANO

PLATELETS REINFORCED WELLBORE CEMENT

Thesis Approved:

Thesis Adviser
Dr. Mileva Radonjic

Dr. Mohammed Al Dushaishi

Dr. Tyler Ley

ACKNOWLEDGEMENTS

I would firstly like to thank my advising committee, Dr. Tyler Ley and Dr. Mohammed Al Dushaishi for their support, review, and feedback. A gracious thank you to my advisor, Dr. Mileva Radonjic, for the great opportunity to work on this project and for providing guidance throughout my graduate academic career. This research is supported by the National Academy of Science and Mathematics Gulf Research Program (NASEM-GRP) grant# 10002358 and the Project Research Team Members: Andrew Bunger group from University of Pittsburgh, Raissa Ferron group from University of Texas Austin, Ipsita Gupta group from Louisiana State University and Pierre Cerasi from SINTEF. A thank you to Dr Dustin Crandall at National Energy Technology Laboratory for his volunteer help and valuable insight. A special thanks to Daniel Bour for bringing this study of graphene addition to cement to our attention as well as providing support and feedback, and to Paul Beasant for providing graphene and additional support. I appreciate the support from Lisa Whitworth and Brent Johnson at Oklahoma State University Microscopy Laboratory. Thank you, Tatiana Pyatina at Brookhaven National Laboratory, for your helpful observations. Special thanks to George King for valuable technical feedback on research and its relevance to field application. Gracious thanks to Dr. Mercy Achang and Dr Guofan Luo for guidance and assistance. I would like to thank Dr. Xiaodan (Sonia) Li for contributing to laboratory testing and Beth Kelly for continual advisement. I am grateful to our Hydraulic Barriers Team at OSU Sai Vamsi Krishna Vissa, Allan Katende, Gabriel Awejori and Dr Fengyang Xiong. Gracious thanks to the postdoc scholars and graduate students from NASEM GRP funded project: Yunxing Lu (PITT), Tamitope Ajayi (LSU), Farzana Rahman (UTA) and especially Hope Asala, who is no longer with us due to the tragic accident. And last but not the least, a thank you to my family for their continual support.

Name: CODY MASSION

Date of Degree: DECEMBER 2021

Title of Study: GRAPHENE NANO PLATELETS REINFORCED WELLBORE CEMENT

Major Field: PETROLEUM ENGINEERING

Abstract: To improve the mechanical performance of wellbore cement under subsurface environments, graphene nanoplatelets (GNPs) are added in various percentages to Class-H cement slurry. Microstructural characterization of cement slurry cured at 90°C and 95%RH indicates GNP modifies the microstructure of hydrated cement by reinforcing pore spaces. As an apparent result, the axial strength increases up to 27%, elastic stiffness decreases as much as 25% when 0.008% to 0.1%bwoc (by weight of cement) of graphene is added to the cement. Furthermore, the overall behavior of GNP- Portland cement paste is more ductile when compared to neat cement paste. From our observations, graphene enhances the flexibility of cement. The improvements would potentially reduce the risks associated with wellbore leakage primarily in plugging and abandonment but potential in other areas such as fossil fuel production, geothermal energy production, and CO2 storage.

TABLE OF CONTENTS

Chapter Page

LIST OF TABLES

Table Page

LIST OF FIGURES

Figure Page

CHAPTER I

INTRODUCTION

Wellbore cement is an integral part of wellbore construction that ensures zonal isolation, holds casing in place, maintains wellbore integrity, prevents loss circulation, and serves as a primary material for Plugging and Abandonment (P&A) of depleted oil and gas wells. Cement integrity and durability are required throughout the lifetime of the well. However, this is not always achieved, especially with wells where hydraulic fracturing and chemically aggressive fluids in the wellbore can lead to cement failure. For P&A, cement plugs should mimic the properties of the original caprock and seal the depleted reservoir for an indefinite length of time, as subsurface fluids could migrate to contaminate water aquifers, agriculture soils, and ultimately the air, causing an overall negative impact on the environment.

To illustrate the relevance of the topic of this study, some of the key published numbers are listed below and supported by Figure 1, indicating the increasing number of wells to be abandoned and methane emissions from 2000-2018:

1. 281 kilotons of methane released by 3.2 million abandoned wells in 2018 (Groom, 2020).

2. Methane gas leakage of oil and gas wells are 60-100% > U.S. Environmental Protection Agency Greenhouse Gas Inventory (GHGI) (Alvarez et al., 2018; Gorchov Negron et al., 2020).
3. Bipartisan senate bill: ~$4.7 billion for P&A projects and clean-up (Gardner, 2021).
4. 2021 infrastructure plan: $8 billion towards P&A (Gardner, 2021)

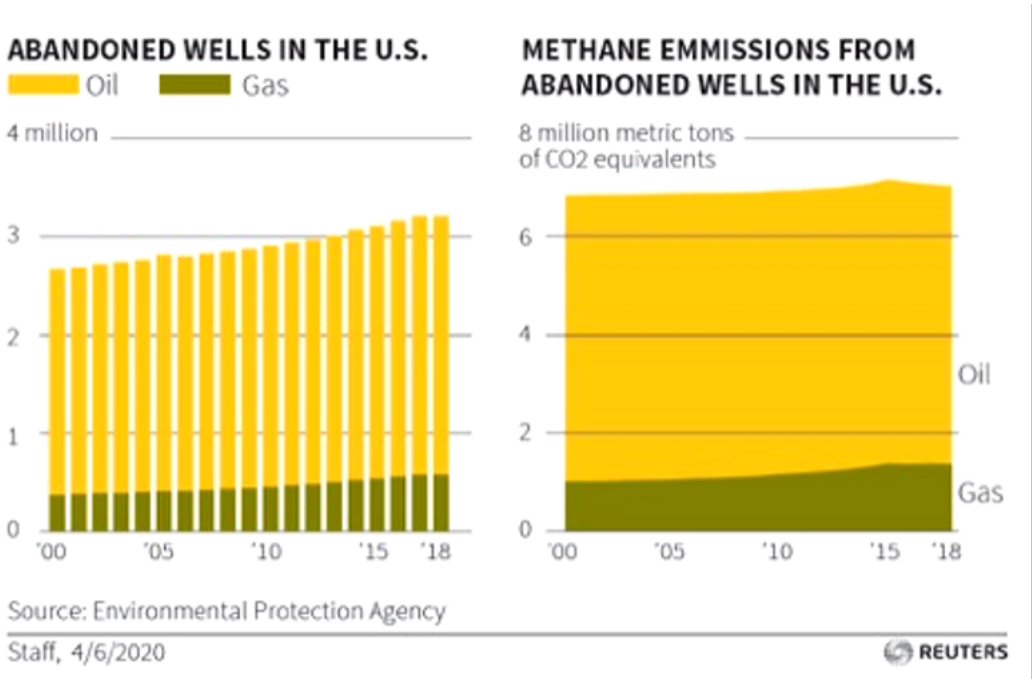

Figure 1 - EPA Published report included charts on oil and gas leaky wellbores, on the left and the conversion of methane emissions to CO2 equivalent (Frazier, 2020).

From a survey of current literature, the use of graphene and its derivatives have shown to provided increased mechanical properties in cementitious materials such as concrete, mortar, and paste. The objective of the study is to investigate the impact of graphene nanoplatelets, as an additive, on wellbore cement mechanical and microstructural properties that translate to the required field performance. Experiments were carried out to evaluate the effects of graphene nano-reinforcement on Young's modulus, shear strength,

and indirect reduction of brittleness. Prior to mechanical testing as well as in post-triaxial load testing, samples were evaluated using materials characterization protocol, which included pore-scale measurement and imaging is carried out to propose micromechanical origins of the observed impacts for GNP on cement properties.

CHAPTER II

REVIEW OF LITERATURE

Ordinary Portland cement (OPC) is the predominant material used to secure the wellbore in primary cementing and for P&A (Rios and Ars, 2021). Approximately 3.7 million wells have been drilled in the United States alone since 1859, and historical records of these wells are not always documented (Allison and Mandeler, 2019). For P&A, cement plugs should mimic the properties of the original caprock and seal the depleted reservoir for an indefinite length of time, as subsurface fluids could migrate to contaminate water aquifers, agriculture soils, and ultimately the air, causing an overall negative impact on the Health, Safety, and Environment (HSE) agenda (Achang et al., 2020). Current P&A cement plugs do not meet the expected geologic seal standards of long-term sealing capacity, currently discussed as 10,000yrs or more. Based on industry field specialists' experiences and the limited report studies, leaky wellbores are evidently one of the problems. The leakage can be present as a result of inadequate primary cementing, its persistence leading to ineffective P&A jobs, causing greenhouse gas emissions and aquifer contamination to a scale that is possibly much larger than is currently reported (Wisen et al., 2020; Alvarez et al., 2018; Gorchov Negron et al., 2020). Leakage can also result from fracturing due to changes in earth stresses as subsurface pressure is altered during subsurface fluids

production or injection. In 2018, it was observed that over 3.2 million leaking wells had released 281 kilotons of methane into the atmosphere (Groom, 2020). Most failure mechanisms of wellbore cement result in fracturing, permeation, and debonding either between the formation-cement or cement-casing interfaces, which would result in micro-annulus leakage (Nelson and Guillot, 2006; Petty et al., 2003; Vrålstad et al., 2019).

2.1. ORDINARY PORTLAND CEMENT

Cement is mankind's solution for developing artificial rock by breaking down natural materials and forming components that will react and harden in the presence of water.

COMPOUND	FORMULA	SHORT FORM	% BY WEIGHT[1]
Tricalcium aluminate	Ca_3Al_2O	C_3A	10
Tetracalcium Aluminoferrite	$Ca_4Al_2Fe_2O_{10}$	C_4AF	8
Belite or dicalcium silicate	Ca_2SiO_5	C_2S	20
Alite or tricalcium silicate	Ca_3SiO_4	C_3S	55
Sodium oxide	Na_2O	N	Up to 2
Potassium oxide	K_2O	K	
Gypsum	$CaSO_4.2H_2O$	CSH_2	5

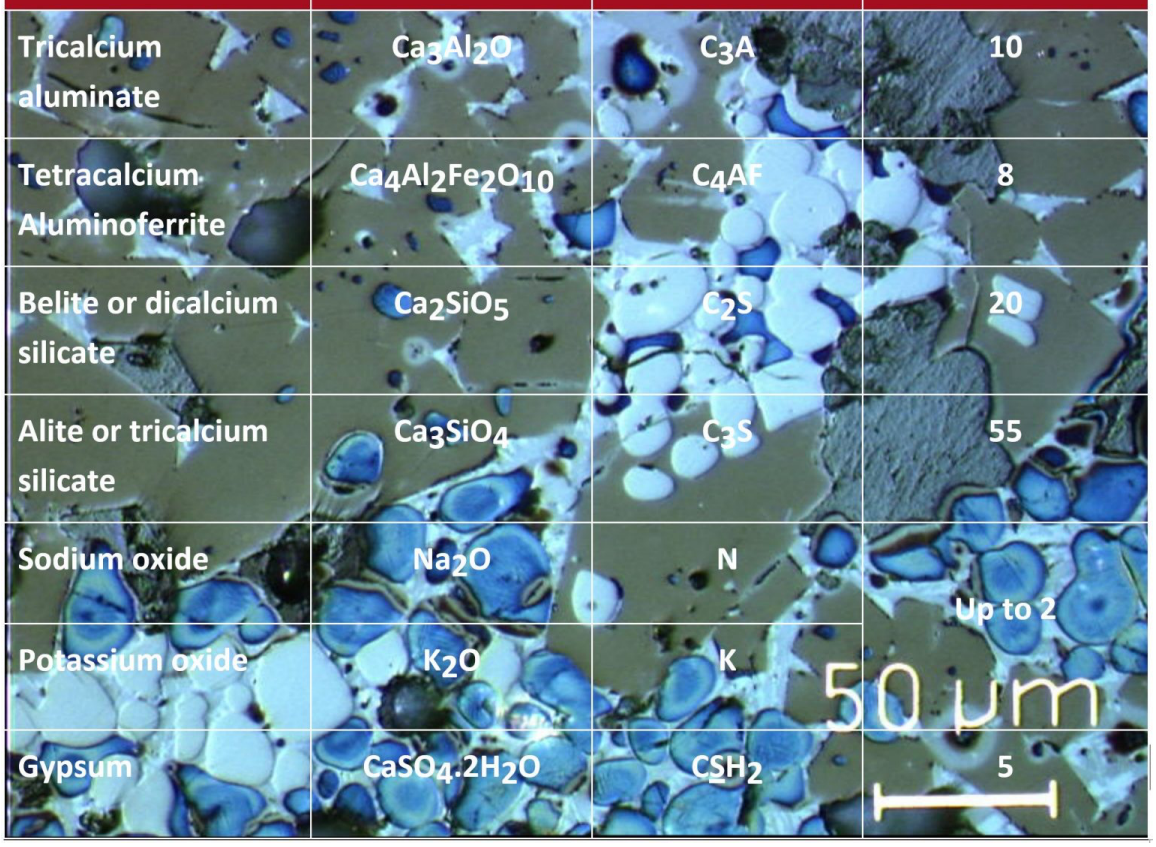

Figure 2 - Cement composition expressed in conventional terminology, chemical formulas and short version used by cement chemists, only representative weights. Actual weight varies with the type of cement (Chemistry and Quality Control Formulas in the Cement Industry, 2020).

Firstly, rocks rich with calcium and silicon, such as limestone and clays, are mined from quarries to be ground, mixed, and burned to manufacture the reactant compounds necessary as ingredients. Cement chemists use abbreviations and shortened notations, such as letters, to indicate oxides abundantly found in cement: CaO=C, SiO_2=S, Al_2O_3=A, Fe_2O_3=F, and similarly H_2O=H. These compounds are primarily, but not limited to, tricalcium silicate (alite, C_3S), dicalcium silicate (belite, C_2S), tricalcium aluminate (aluminate, C_3A), calcium sulfate (anhydrite, gypsum), and tetracalcium aluminoferrite (ferrite, C_4AF) (Neville and Brooks, 2010; Fink, 2012). Other compounds or ratios of these may be changed in the mixing process to alter the properties of the final cement product. When water is added to this mixture, an exothermic chemical reaction takes place called cement hydration that results in a hardening and strengthening of the material that can be used in a variety of applications. In the beginning of the hydration process, water begins to break down the compounds where calcium ions and silicon ions are pull into solution. New compounds form these ions begin to nucleate on the surface of remaining particles. Calcium silicate hydrate (CSH) and calcium hydroxide (portlandite, CH) form primarily from C_3S and C_2S. C_3A and gypsum react together to form small needle-like ettringite crystals. More chemical products are formed and grow on the grain surfaces as water diffuses into and reacts with the unhydrated particles. CSH and ettringite begin to form a

matrix as they grow to connect all the particles together, forming a solid mass that can begin to hold strength (Barnes and Bensted, 2002), as shown in Figure 3.

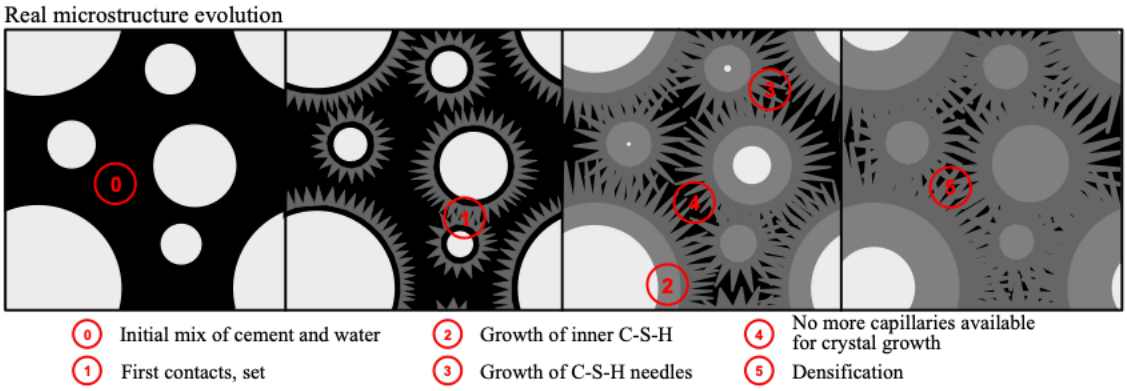

Figure 3 - OPC hydration shown schematically, and not to scale for clarity of mechanisms (Dunant et al., 2020).

Cement and concrete terminology are generally based on what is mixed in with addition to cement and water, also referred to as cement paste. Fine aggregates can be added and are referred to as particles typically larger than 75 microns but smaller than 4.75mm, such as sand, to form what is called cement mortar. Furthermore, coarse aggregates, such as gravel and crushed stones, are typically particles larger than 4.75mm to create the abundantly used material of concrete (Mehta and Monteiro, 2006). The use of these similar materials is highly dependent on the application and desired properties. Construction of buildings, bridges, and other structures are commonly made of concrete due to the workability, durability, and strength of the material as well as the available space. Whereas cement paste is generally used in wellbore construction and P&A for its pumpability and sealing the confining micro annuli due to its minimum particle sizes.

Wellbore cement slurries usually contain various additives or admixtures that can be used to modify the slurry or hardened cement characteristics or properties such as

rheology, hydration time, fluid loss, density, strength, chemical resistance, and more (Bensted and Barnes, 2008). Pozzolans are commonly used in cement and concrete mixing and can be derived from naturally forming deposits of volcanic ash or produced artificially as fly ash and blast furnace slag that industrial waste products. These are referred under the category of supplementary cementitious materials (SCM) as they are rich in silicates and aluminates and provide a means to maintain or aid the hydration reactions in cement while reducing the amount of cement powder used.

To further improve the performance of cementitious materials, other materials can be used to create an overall composite that primarily improves mechanical and durability properties. This is seen on large scale with the common use of steel rods or bars being placed within concrete. This can also be observed at a smaller scale with the use of fibers as reinforcement. These fibers can be composed of steel, plastic, glass, or even materials from nature (Mehta and Monteiro, 2006; Neville and Brooks, 2010). The addition of these can allow for higher early strength and toughness of the material, while also reducing or slowing of the fracture propagations once failure occurs (Brown et al., 2002).

The advances in the ability and availability to examine and manufacture nanomaterials within the last few decades has swept the scientific research community. As a result, the use of various nanomaterials have and are currently being investigated for the use in cement and concrete to enhance the performance of the materials. A few of the nanomaterials that have shown high potential in this field are nano-silica, nano-CSH, and nano-carbons (Zhao et al., 2020; Sobolev et al., 2006).

2.2. SHALE CAPROCK

To understand the potential natural problems and engineering solutions for P&A, the downhole formations must firstly be understood. As cementing is a method to artificially produce rock-like materials, for P&A this in turn means evaluating the shale caprock that had originally sealed the formation for thousands of years. Engineering the cement plug to perform similarly and mimic the caprock is a possible direction toward promising results.

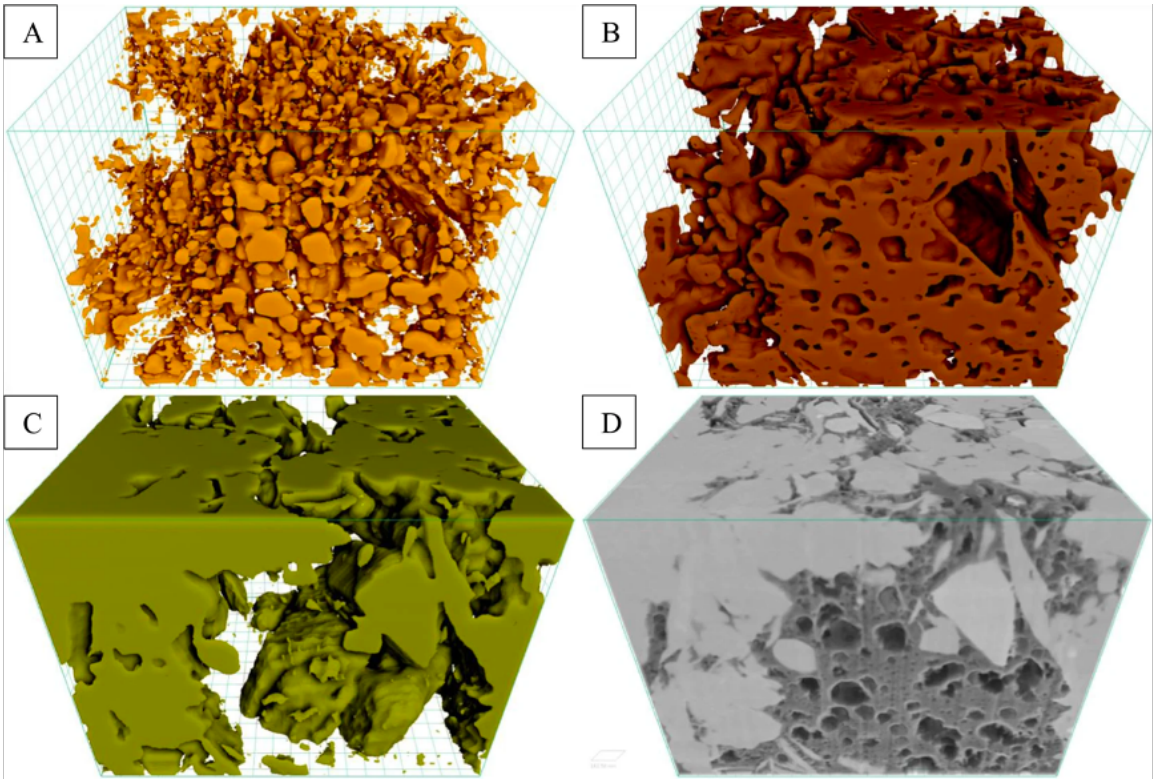

Figure 4 - Visualization of segmented (A) pores, (B) organic matter, and (C) mineral phases present within digital rock 3D model reconstructed from (D) FIB-SEM nano-tomography image dataset, from Goral et al. (2020).

The mechanical properties are the first key aspect to observe, as wellbore conditions consist of high temperatures and pressures that cause stresses and potentially fractures in

any material within the environment. Shale caprocks are relatively ductile with lower elastic moduli in relation to other formations. From data and sampling of multiple wells from the Draupne and Heather shale formations in the North Sea, Rahman et al. (2020) had characterized the mechanical properties of elastic modulus and poissons ratio to approximate range of 5-40 GPa and 0.27-0.41, respectively.

Likely, using micromechanical tool of micro indentation the elastic modulus of Marcellus and Pottsville shales showed a range of measured values from 0-70 GPa in softer regions, and greater than 120 GPa in harder regions (Du et al., 2020). These variations were largely to do with the material microstructure and composition such as number of rigid grains, grain size and distribution, and clay and organic content. Liu et al. (2020) additionally observed the bedding angle dip of the formation had altered the strength and fracture patterns while under triaxial loading and reported an ultimate stress range of approximately 125-227 MPa and 200-290 MPa for unconfined and confining pressure of 30 MPa, respectively. Shales with lower clay content and higher combined contents of quarts, feldspar, and carbonates are typically of interest for hydraulic fracturing. This is because more clay and organic content within the formation lower the brittleness and elastic modulus of these rocks (Sone, 2012; Jamilur Rahman et al., 2020).

Petrophysics in the wellbore environment is another important characteristic of the formation and downhole environment. The sealing caprock has prevented the migration of subsurface fluids for thousands of years to maintain the reservoir, which can consist of oil, natural gas, and brine. Any leaking or permeation through this barrier would cause fluid and pressure loss, resulting in no reservoir to produce from. To prevent this the caprock is tight with low pore connectivity and the sealing capacity is generally controlled by the

porosity, permeability, and thickness (Schowalter, 1979; Downey, 1984; Vavra et al., 1992). The pore size distribution shale caprock formations are typically measured with mercury intrusion to be in the nanoscale range with pore sizes 0.025 microns or less (Olabode and Radonjic, 2014, Chen et al., 2014). For pore connectivity and fluid penetration, the permeability and hydraulic conductivity of shale is less than 1 millidarcy and 10^{-12} m/s, respectively (Shipton et al., 2005; Kvamme and Liu, 2009; Chen et al., 2014).

To evaluate why the shale caprock behaves this way and has the mechanical and petrophysical properties that can withstand harsh downhole conditions, analysis at the microscale must be achieved. The microstructure and minerology can explain the low brittleness and permeability used for sealing of the reservoir. As many natural occurring formations, shales are heterogeneous that consist of three notable categories: clays and organic material, quartz and feldspar, and calcium carbonates. These heterogenous rocks are tightly packed formations with fine grain sizes, ranging from 10-200 microns in quartz, feldspar, calcite, and illite down to less than 2-micron grains with clay minerals (Du et al., 2020).

The most effective shale caprocks are formations containing fine grain clay-based siliciclastic, anhydrites, gypsum, halites, and/or organic rich are usually selected as the caprocks to ensure the effectiveness. (Olabode, A., & Radonjic, M. 2013). Shales seen as caprocks generally have a higher clay and organic content that creates a tight, soft pore media, whereas hydraulic fracturing shales have higher contents of quartz, feldspar, and calcium carbonates (Na et al., 2017). These clays have been found to decrease the brittleness and elastic modulus of the overall material (Sone et al., 2012; Jamilur Rahman et al., 2020).

2.3. PLUGGING AND ABANDONMENT OF OIL AND GAS WELLS

An ideally permanent wellbore cement should provide long term integrity through providing a non-shrinking material that is ductile, chemically resistant to the wellbore fluids, and exhibits good bonding to the casing and the rock formations (Aasnes, 2017). Studies have been conducted on well integrity on an international scale and concluded that integrity failures are of low risk for a few decades (O'Kane, 2014), but little research has been aimed at a timespan more than this and it has been observed that harmful gases or fluids will continue to leak into the environment (King and King, 2013). Current and past P&A cement plugs may not meet the expected geologic seal standards of long-term sealing capacity, and in some cases, leakage is present as a result of inadequate primary cementing and can persist and prevent effective P&A jobs. This is an increasing problem as a large number of oil and gas wells will be decommissioned due to their productive and economic inefficiency (Warne, 2004; Liversidge et al., 2006; Kaiser, 2015). Out of approximately 15,500 wells in the Gulf of Mexico between the years of 1973-2003, the United States Minerals Management Service data had reported 43% of those wells had sustained casing pressure (high pressurization due to subsurface fluids leakage by the cement sheath and into the well annulus) that poses a threat to safety, the environment, and the well itself (Brufatto et al., 2003; Rusch et al., 2004; Bois et al., 2011).

Leakage can also result from fracturing due to changes in earth stresses as subsurface pressure is altered during subsurface fluids production or injection. Most failure mechanisms of wellbore cement, result in fracturing, permeation, and debonding either between the formation-cement or cement-casing interfaces, which would result in micro-annulus leakage (Nelson and Guillot, 2006; Vrålstad et al., 2019; Petty et al., 2003), as

shown in Figure 5. Many offshore wells can experience more extreme conditions than typical conventional wells, such as high pressures and high temperatures (HPHT) that require thicker slurries and higher quality control, imposing additional problems for P&A (North et al., 2000). These conditions can cause mechanical stress and strain on the cement plug that could lead to a progressively greater leakage even with an adequately initial cementing (Lecampion et al., 2013; Zeng et al., 2019; Wise et al., 2020).

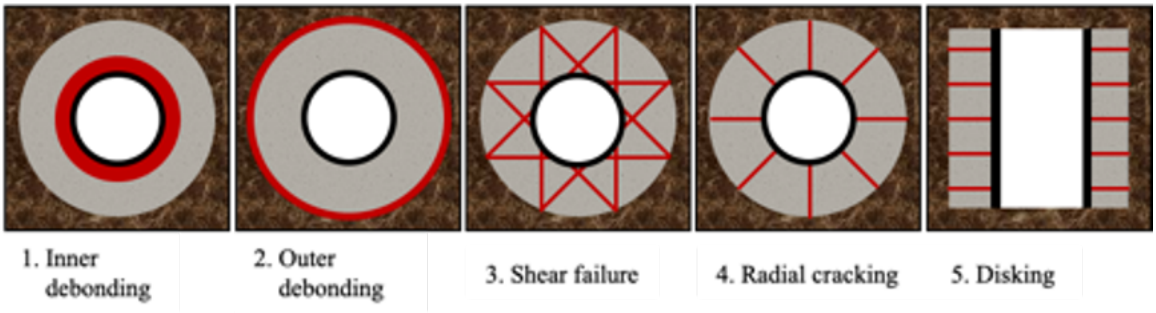

Figure 5 - Annular wellbore cement leakage mechanisms indicated by red. (1) debonding between cement and outside of the casing (2) debonding between cement and the formation rock (3) shear failure through the cement plug (4) radial cracking from the casing through the plug, to the rock (5) cement horizontal fractures known as disking. Modified from Petty et al., (2003).

Wells in the Gulf of Mexico region reach depths greater than 4300 ft (1300m) and generally see and bottomhole pressures of 7000-7500psi (Pakulski et al., 2005) and temperatures ranging from 90 to 200+°C (194 to 392+°F) (Bello, 2014), although deeper and more harsh wellbore conditions are not unlikely. Cement slurries of densities ranging between 16 and 18.5 pounds per gallon (ppg) with water to cement ratios between 0.38 and 0.46 (Fink, 2012) are typically used to create plugs that are between 300-900 ft (90-275 m) in thickness (Olutimehin and Odunuga, 2012; Bogaerts et al., 2013) to ensure a proper

barrier. Plugs outside of these bounds could have a higher possibility to failure due to contamination of the spacing fluid if shorter, and extended setting time if longer (Moraes et al., 2013).

2.4. GRAPHENE NANOPLATELETS AND GRAPHENE DERIVATIVES

Graphene is made of carbon atoms in a flat two-dimensional hexagonal lattice that link up to create a honeycomb-like sheet structure that is thinnest and the strongest material known at this time (Horst et al., 2018). The International Union of Pure and Applied Chemistry defines graphene as "a single carbon layer of the graphite structure, analogous to a polycyclic aromatic hydrocarbon of quasi-infinite size" (McNaught and Wilkinson, 1997), and has Young's modulus of approximately 1 TPa (Lee et al., 2008). The term graphene has been used for various compositions up until 1985 in a publication where Boehm et al., 1985, began a standardization to distinguish it from other graphite intercalation compounds (GICs). They initiated the distinction of GICs graphite, graphene, graphene oxide (GO), and reduced graphene oxide (rGO). Pure graphene has impressive intrinsic mechanical, thermal, electrical, and optical properties that have high amounts of potential in a large range of applications.

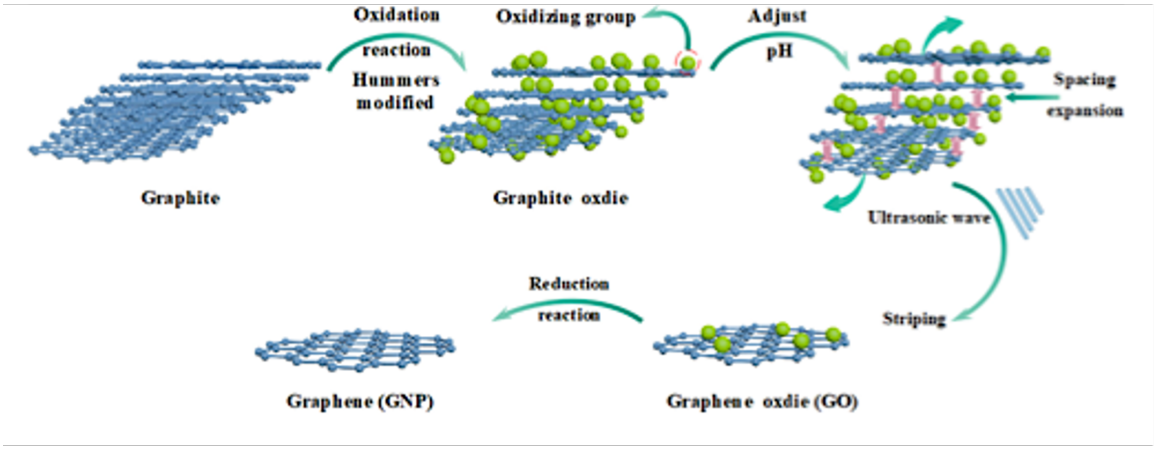

Figure 6 - Conceptual models of graphene and derivatives structures (Han et al., 2021).

Graphene oxide has a lower carbon percentage as it is derived from oxygenated graphite while graphene has the largest carbon content. The increased percentage of oxygen in GO causes imperfections and defects on the sheets that lead to weakness and reduced properties, but it is more cost-effective in large-scale synthesis (Zhu et al., 2010). In attempts to reduce these impurities, GO sheets are treated by chemical, thermal, or electrochemical reduction to minimize the defects thus creating rGO (Tiwari et al., 2020; Botas et al., 2012; Gadgil et al., 2016). rGO sheets still show reduced properties such as strength and conductivity when compared to pure carbon graphene. For example, GO and rGo can exhibit a reduction in Young's modulus of 250 GPa when compared to pristine graphene's modulus of 1TPa (Kong et al., 2019). For the last 25 years, the scientific community has shown great interest in this material and researchers are investigating the applications in different fields.

2.5. GRAPHENE AND DERIVATIVES IN CEMENTITIOUS MATERIALS

Graphene in the oil and gas field is being researched as an additive in drilling fluids to enhance lubrication, in anti-corrosion coating of metal, and in enhancing cement properties (Neuberger et al., 2018). Mokhtar et al., 2017 have shown that the addition of graphene nanosheets and their derivatives increases the rate and heat of hydration translating to more complete hydration of clinker and improved pore structure, thermal stability, and mechanical properties of the cement. A study conducted by Baomin and Shuang, 2019 on the mechanisms of graphene nanoplatelets (GNP) in cement hydration and pore structure suggests a 0.06%bwoc addition reduces compressive and flexural strength to 11.0% and 27.8% respectively, after 28 days of hydration when added to ordinary Portland cement. They used X-ray diffraction (XRD) and thermal analysis (TG/DTG) and demonstrated that the GNP could accelerate the degree of hydration and increase the number of hydration products, especially at an early age. Other studies state that GO acts as a template for cement hydration to occur on and produce flower-like crystal growth on the platelet surface (Lv et al., 2013; Lv et al., 2014; Yang et al., 2017). Pan et al., 2015 suggest that the GO sheets increase mechanical properties by blocking crack propagations.

Table 1 - Collection of relevant literature studies for the use of graphene and graphene derivatives reinforcing cementitious materials from Han et al., 2021.

Researcher	Graphenematerial type	Physical properties		Adding amount/ %	Cement type	External additive	Aggregate type
		Number of layers	Specific surface area ($m^2.g^{-1}$)				
Du et al. [94,98–100]	GNP (TC 307)	<10	352	5–20, 5 increased (mass of cement)	Ordinary Portland cement (OPC)	Superplasticizer (Darex Super 20)	Natural sand (maximum size: 2.36 mm, fineness modulus: 2.95)
	GNPs (exfoliated from FG A3775)	≥10	24	2.5–7.5, 2.5 increased (mass of cement)	OPC	Superplasticizer (Darex Super 20)	Natural sand (density:2.65, fineness modulus:2.95
	GNPs (exfoliated from FG A3775)	≥10	24	0.5–2, 0. 5 increased (mass of cement)	OPC (CEM I 52.5 N)	Superplasticizer (Darex Super 20)	Natural sand (maximum size: 4.75 mm) and coarse aggregate (maximum size: 19 mm)
	GNPs (exfoliated from FG A3775)	≥10	24	0.25, 0.5, 1, 2 and 4	OPC (CEM I 52.5 N)	Superplasticizer (ADVA-181 N)	––
Le et al. [101]	GNP (TC 307)	<10	352	5–20, 5 increased (mass of cement)	OPC	Superplasticizer (Darex Super 20)	Natural sand (maximum size: 2.36 mm, fineness modulus: 2.95)
Pang et al. [102]	GNP (TC 307)	<10	352	1.2–4.8, 1.2 increased (volume of the composites)	OPC	Superplasticizer (Darex Super 20)	Natural sand (maximum size: 2.36 mm, fineness modulus: 2.95)
Dalla et al. [103]	GNP	–	–	0.2 and 0.4 (mass of cement)	OPC (I 42.5 t)	Superplasticizer (Viscocrete Ultra 300 and 600)	Natural sand
Jin et al. [104]	GNP	1–5	360–450	2 (mass of cement)	OPC (P.II 42.5 N)	Polycarboxylate Superplasticizer (PC)	––
Tragazikis et al. [105]	GNP	<10	–	0.2–0.4 (mass of cement)	OPC (I 42.5 t)	Superplasticizer (Viscocrete Ultra 300 and 600)	Natural sand
Yanturina et al. [106]	GNPs	<10	–	0.01 (mass of cement)	OPC (CEM I 42.5 N)	Superplasticizer (PS 160 Plv)	––
Tong et al. [95]	GNPs (GMs and GCs) and GOs (GOMs and GOCs)	–	GMs: 150 and GCs: 500	0.1 (mass of cement)	OPC	Superplasticizer	Sieved sand
Lv et al. [107,108]	GOs (homemade)	–	–	0.01–0.05, 0.01 increased (mass of cement)	OPC (Shengwei 42.5R)	PC	Standard sand
	GOs (homemade)	–	–	0.01–0.06, 0.01 increased (mass of cement)		PC	
Gong et al. [109]	GO (homemade)	–	–	0.03 (mass of cement)	OPC (Type I)	–	–
Li et al. [110,111]	GO (homemade)	–	–	0.3–2 (mass of cement)	OPC (Type II)	CNT (Single-walled) and PC	Standard sand
	GO (homemade)	–	–	0.02 and 0.04	OPC (Type I)	PC (ADVA 210) and powder defoamer (Agitan P803)	High-purity silica sand
Mohammed et al. [112]	GO	–	–	0.01, 0.03 and 0.06(mass of cement)	OPC (GP)	Water reducer (HWR)	Standard sand
Sharma et al. [113]	GO (homemade)	–	–	0.125, 0.25, 0.5 and 1 (mass of cement)	OPC (Grade 43)	PC (Glenium)	Indian Standard sand
Pan et al. [114]	GO (homemade)	–	–	0.05 (mass of cement)	OPC (Type I)	–	–
Horszczaruk et al. [115]	GO (homemade)	–	–	3 (mass of cement)	OPC (CEM I 42.5R)	–	Standard sand
Wang et al. [116,117]	GO (homemade)	< 10	376.53	16.7–43.3 (mass of cement)	OPC (Type 52.5R)	–	–
				0.01–0.05, 0.01 increased (mass of cement)		–	–
Liu et al. [118]	GNPs (SE1231) and GOs (SE2430)	≥10	191.8	0.025, 0.05, 0.1, 0.2, 0.4, 0.8, 1.6, 3.2 and 6.4 (mass of cement)	OPC (Type 52.5)	PC	Sieved dry sand
Long et al. [119,120]	GO	< 10	–	1, 0.33 and 0.11 (mass of dispersing agents)	OPC (Type I)	Water reducer (N-HRWR: Sika KS-20, P-HRWR: TMS-YJ-1 and air-entraining admixture (AEA): BASF MicroAir)	–
	GO	< 10	–	0.125 and 0.25 (mass of cement)	OPC (PI 42.5R)	PC (RMC-3 and CP-WRM50)	
Li et al. [121]	GO	< 10	–	0.02–0.08, 0.02 increased (mass of cement)	OPC (Type I)	–	Tricalcium silicate (C_3S)
Mokhtar et al. [122]	GO(homemade)	–	–	0.01–0.05, 0.01 increased (mass of cement)	OPC	–	–

The addition of graphene, one of the strongest materials known today, with high tensile strength, Young's modulus, electrical and thermal conductivity, low density, and hydrophobic nature (Dreyer et al., 2010; Tiwari et al., 2020), has the potential to improve wellbore cement properties based on its impact on other composite materials. To be implemented in the field, new additives to wellbore cement have to be investigated and verified using microstructural characterization and mechanical testing at reservoir conditions, as well as rheological properties that are critical for effective downhole placement. One objective of this paper is to report the findings on the impact of graphene nanoplatelets on the wellbore cement properties such as strength and modulus of elasticity with the ultimate goal to understand the mechanisms of how graphene nanoplatelets contribute to cementing hydration and overall micro-architecture of the matrix. These properties are critical for challenging well environments found in high-pressure/high-temperature (HPHT) environments, offshore deep-water wells, or onshore horizontal unconventional wells, in both primary cementing and P&A. Similar demands are expected from geothermal wellbore cement, where low pH and more extreme temperature variations are expected.

CHAPTER III

METHODOLOGY

Graphene was firstly received in 3 different types or grades with names of Platinum, Black, and Diamond with descriptions provided by the material data sheet and provider as follows. Platinum consists of graphene nanoplatelets by inert graphite exfoliation of fewer than 7 layers with 87% between one to three layers, with greater than 95.5% carbon content and less than two percent oxygen content. These platelets are specified at a particle size range of 100nm to 10μm. Black is formed from the refinement of biochar consisting of single and multi-layer nanoplatelets as well as amorphous carbon. Carbon content consisting of greater than 91% and less than eight percent oxygen content. Diamond was described similarly to Black in processing, with further stages to refine the product. These graphene materials were examined as received for microstructure, chemical composition, and stability by methods of transmission electron microscopy (TEM), scanning electron microscopy (SEM), and energy-dispersive x-ray spectroscopy (EDS). After this analysis, the graphene chosen for use in this study and to be added to the wellbore cement was Platinum. It was added to Class-H cement in 0% (referred to as neat or control), 0.008%, 0.016%, 0.05%, and 0.1% by weight of cement (bwoc), along with D-air 5000, dispersant CFR-3, and bentonite to make cement at a slurry of density 16.4ppg (1.94g/cm^3) and water

to cement ratio of 0.38. Tests conducted on the cement samples to evaluate cement microstructural and mechanical properties include strength, as well as microstructural characterization, using Scanning Electron Microscope (SEM), Energy Dispersive Spectroscopy (EDS), and Micro/Nano Indenter.

3.1. TRANSMISSION ELECTRON MICROSCOPE

TEM images were taken of the graphene as received to investigate the microstructure of thin individual sections. This was done by suspending a small quantity, approximately 0.1gr, of GNP in isopropyl alcohol and sonicating for approximately 2 minutes. A very small amount of 8uL was then dropped onto a holey carbon grid using a micropipette, waiting 60 seconds, and soaking up the excess alcohol. The holey grid with graphene is then imaged with the Model JEM-2100 TEM microscope at 200kV and a magnification of 25,000x.

3.2. SCANNING ELECTRON MICROSCOPE

Graphene was prepared for SEM imaging by attaching carbon tape on SEM stubs and depositing approximately 0.1gram of graphene onto the adhering tape. No coating was used as the graphene is composed primarily of carbon and had no issues with sample charging. Imaging with Thermofisher Scios2 SEM, using secondary electron (SE), backscatter electron (BSE), and EDS, between 5-25keV and acquisition time of approximately 10-30 minutes for elemental maps.

3.3. CEMENT MIX DESIGN, PREPARATION, AND CURING

Portland cement-based Class-H wellbore cement was used as the dominantly used API cement for HPHT in the Gulf of Mexico. Defoamer, D-Air 5000, cement friction reducer CFR-3, bentonite, cement, and deionized water were all measured to make a calculated 16.4ppg (1.94 g/cm^3) slurry. Following API Standard RP-10B procedures for mixing of well cement slurries, the measured quantity of water was poured into the blending container and a Waring model CB15N blender then turned on to a rotational speed of approximately 4,000RPM setting, where graphene was added and dispersed in the water for 1 minute. The measured Class-H cement powder, D-Air 5000, CFR-3, and bentonite had been dry blended by hand and added, in a span of 15s, to the water at the 4,000 RPM inside the blender. After these 15s, the blender speed was steadily but quickly increased to a setting of 12,000RPM, where the slurry was then mixed for 35s. With the mixing finished, the blender was then turned off and the slurry immediately poured into the curing molds.

Brass molds of diameter and length 2.54 x 7.62 cm (1 x 3 inch) and 3.05 x 6.10 cm (1.2 x 2.4 inch) sizes were prepared by lubricating the interior with WD-40 water-resistant silicone lubricant and letting it soak for at least 5 minutes before flipping the molds over and letting excess lubricant drain out for approximately 5-10 minutes. Once slurry mixing had been completed, it was poured into each mold by use of an icing pouring bag with an attached pointed tip to reduce air bubbles poured into molds as well as reduce wasted slurry. Molds were shaken while cement slurry was poured to reduce air bubbles trapped in the cement. After molds were filled, they were further shaken and prodded with a slim metal rod to promote any trapped air bubbles to rise to the surface, as such defects would have significant consequences on materials characterization and testing results.

The molds were covered with clingfilm wrap to prevent any fluid loss by evaporation and set to hydrate at ambient conditions for 24 hours. After 24 hours, they were demolded and immediately submerged in calcium hydroxide solution of ~pH13 and covered with aluminum foil and sealed with saran wrap. The samples in solution were placed in an ESPEC Global-N environmental chamber and cured at 90°C and 95% relative humidity to simulate subsurface wellbore conditions. Samples that had been dried after this curing had resulted in a dry density of 14.9 ppg hardened cement.

Two batches of cement samples had been made and tested throughout the duration of this research study. The first batch, Batch1, was made with graphene at percentages of 0%, 0.05%, and 0.1%bwoc. Samples were cured at the above conditions for 21 days prior to testing. The second batch, Batch2, was with the purpose to investigate how lower quantities of graphene at percentages of 0%, 0.008%, 0.016%, and 0.05%bwoc perform at 28 days in the simulated environmental conditions.

Table 2 - Summary of slurry designs for the addition of 0-0.1% graphene nanoplatelets to cement slurry at 16.4ppg.

Materials used	Neat cement (grams)	0.008% GNPs (grams)	0.016%GNPs (grams)	0.05% GNPs (grams)	0.1% GNPs (grams)
Class-H cement	1255.06	1254.98	1254.90	1254.55	1254.05
Water	481.57	481.56	481.54	481.46	481.36
Graphene	0.00	0.10	0.20	0.63	1.25
D-Air 5000	3.14	3.14	3.14	3.14	3.14
CFR-3	3.77	3.76	3.76	3.76	3.76
Bentonite	25.10	25.10	25.10	25.09	25.08

3.4. SCANNING ELECTRON MICROSCOPY OF HYDRATED CEMENT

Hydrated (set) cement cores were first wet cut using deionized water and a band saw to trim uneven edges and create flat parallel ends. 1x3 inch samples were cut to a length of approximately 0.5 inches and used for SEM and indentation were polished starting with a 600-grit silicon carbide (SIC) abrasive disc used for grinding to remove initial deformations. After each step, the surfaces are inspected under the microscope to ensure a uniform scratch pattern. Grinding induced deformation is removed using 6 μm diamond suspension on Gold Label polishing cloth and 1 μm diamond suspension on White Label polishing cloth, with Purple-Lube. Samples are sonicated with isopropyl alcohol in a tabletop sonicating bath for five minutes at the end of each step to remove fragmented cement, residual diamond suspension, and colloidal silica. The polished samples are then dried overnight in a drying oven at 50°C, and further water removal is done prior to indentation, SEM, and EDS.

Polished and fractured cement, were characterized with SEM and EDS. A flat and smooth surface for the polished samples of cement was achieved by following the polishing procedure listed above. Polished and fractured cement surfaces were iridium-coated to prevent charging effects before imaging with Thermofisher Scios2 SEM, using secondary electron (SE) at 20keV and backscatter electron (BSE) at 12keV, and EDS, using 12keV and acquisition time of approximately 30 minutes.

3.5. X-RAY FLOURESCENSE

The raw material samples were analyzed for chemical composition of cement powder and additional additives before being mixed. A plastic cylinder of approximate size

1-inch diameter and 0.5-inch height was filled with each raw material. Samples were placed inside the Edax/Ametek Orbis PC XRF and test setting of 50kV, 1000μA, and 5 iterations were used.

3.6. X-RAY DIFFRACTION

Hydrated cement samples were crushed and powdered and sieved through a 95-micron sieve. Testing was conducted on a Bruker D8 Advance x-ray diffractometer at a voltage of 40kV and current of 40mA. Step rate was conducted at 0.5 seconds per step and a step size of 0.01 degrees.

3.7. RAMAN MICROSCOPE

Raman spectroscopy provided information on material chemical composition and phase identification and can be used as a nondestructive technique regardless of the condition of physical state of the samples. Chemical bonds within the material interact with the laser light and emit unique signatures that can be observed as peaks within the spectrum. Spectrums for graphene and neat cement were obtained using a Witec alpha300R containing both 532nm green and 785nm red lasers. Approximately 0.1gram of as received graphene nanoplatelets were placed on a glass slide and analyzed using a the 532nm laser with a power of 2volts and an integration time of 1s. Polished cement samples were analyzed using the same laser at a power of 4.2volts and an integration time of 2s.

3.8. COMPUTED X-RAY TOMOGRAPHY SCANNING

The samples used for triaxial compression testing were scanned to observe the fracture patterns and behavior for each sample set using a North Star Imaging M-5000 Industrial Computed Tomography (CT) scanner. The samples were received at the National Energy Technology Laboratory submerged in the hydraulic oil that they were tested in, and they were not removed from the oil for scanning. 2D radiographs were captured with the Feinfocus FXE source at 185 kV and 200 mA, with 12 frames averaged for each radiograph. A 360-degree rotation of the sample was performed with 1440 images captured. These scans were reconstructed with North Star Imaging efX-CT® software and the resultant 3D images had a voxel resolution of (32.9 mm)3. Image segmentation of the open voids and fractures from the cement matrix was performed using pixel segmentation with ilastik (Berg et al., 2019). Further post-processing of the images and visualization was performed using ImageJ/FIJI (Schindelin et al., 2012).

3.9. POROSIMETRY

Within the subsurface environment, petrophysical properties such as porosimetry are important to understand solid material interactions with wellbore fluids. The porosity indicates the amount or volume percentage a fluid may occupy within a sample. Other observations such as pore radius and distribution can also be measured. Corelab™ Ultra-pore porosimeter was used to find the porosity of the 1 x 3 inch samples. Cement samples were placed in the matrix cup along with any calibrated disks needed to fill the remaining volume. Helium gas flows into a tank of known volume and pressure of a specified ~200psi. Once this new pressure is stabilized, the pressure difference in pressure is used

along with the known respective sample dimensions to find the pore volume of the sample using Boyle's law, with the assumption of an ideal gas, to calculate porosity, grain volume, and bulk density.

Porosimetry of neat and 0.05%GNP cement had then been conducted using mercury intrusion porosimetry (MIP), a test conducted by Corelab™. Samples were cut to a length of 2.54cm (1in) and were then cleaned and dried. Samples were immersed in mercury in a pressure-sealed chamber with the pressure of the surrounding mercury gradually increased from 5 up to 55,000psia. The relationship of injection pressure to mercury saturation was used to calculate parameters of porosity and pore throat size distribution.

3.10. PERMEABILITY

Another important petrophysical property is permeability. This is a measurement of the ability of a fluid to penetrate and flow through the interconnected pores in a material. The samples for the helium gas porosimeter were then used to evaluate gas permeability using a Corelab™ Nano-K^{TM} permeameter. The measured length and the diameter of the cement cores were recorded, and the sample was placed in the confining pressure cell. A confining pressure of 2000psi was applied and helium gas with an upstream pressure of 1, 2, and 3psi were applied to the core system. Time taken for outlet pressure to reach 4.5mmHg were used to find the intrinsic permeability coefficient, k, by using Darcy's Law modified for a compressible gas or fluid.

3.11. INDENTATION

The mechanical performance of wellbore cement is one of the most crucial aspects when in consideration of the stresses created by downhole pressure. Micro-indentation was first used to evaluate the mechanical properties at the microscale. Hydrated cement core samples were cut and polished using the procedure in Section 3.4. After the cutting and polishing procedures, the resulting dimensions were 1in squares and approximately 0.25in height. Indentation of samples was conducted on a Nanovea PB1000 Hardness Tester using the micro indentation option. A micro-Vickers diamond tip with a tip angle of 90 degrees, the elastic modulus (E_i) = 1140 GPa, and Poisson's ratio (v_i) = 0.07 was used and calibration of the system in accordance with ASTM Standard E2546 using a finely polished stainless-steel calibration sample with known properties. For this experiment, 25 indentations were taken per sample in a 5x5 matrix configuration each with a spacing of 400μm and tested at a maximum load of 5 N, loading, and unloading rate of 10 N/min, and creep time of 300s were used. The load vs depth was then plotted and analyzed using the loading and unloading curves according to ASTM E2546. Young's modulus was calculated using the 10-50% portion of the unloading curve.

3.12. TRIAXIAL COMPRESSION TEST

Triaxial testing was used to determine the axial stress and stiffness of the cement in relation to its application of the wellbore environment under conditions of both temperature and pressure. The triaxial tests are performed in a temperature-controlled Hoek-type triaxial compression cell, which consists of three main parts: axial loading system, confining stress system, and temperature-control system. Cement cylinders of 1.2-

inch diameter and 2.4-inch length were used. The experimental approach entails applying confining pressure and temperature replicating downhole conditions while simultaneously imposing the increasing axial (deviatoric) load until the specimen fails. The deviatoric loading is controlled by an INSTRON-600DX load frame, which can provide up to 600KN. The confining stress is maintained by a high-pressure syringe pump (ISCO-260D), which is also allowing precise measurement of the volume change of the specimen associated with a given confining stress up to 70 MPa. The temperature is provided by wrapping the Hoek cell with the heating tape that can provide a controlled temperature up to 180°C. In the experimental procedure for performing the triaxial tests, the cylindrical specimen is kept in fully saturated conditions until the test starts. Then the core specimen is placed into the membrane/core holder, which is specially designed to attach to the cell so that the whole system remains airtight. After the core holder with a specimen is placed into the Hoek cell, hydraulic oil is pumped into the space between membrane and cell so the lateral pressure can be provided. The specimen is axially enclosed by two steel loading plates (top-loading plate and bottom spacer). The top vertical piston of the load frame will directly contact the top-loading plate so the deviatoric load can be applied to the specimen.

By using heating tape wrapped around the Hoek cell, the temperature of the cell can be slowly increased to the targeted temperature, i.e., 90℃, over two to three hours at a low hydrostatic pressure of 1.4 MPa. Note that by requiring hours for the heating process, it is possible to drive some evaporation of pore fluid so that the specimen deviates from fully saturated conditions. Furthermore, pore pressure might be increased during confinement due to coupling between the pore fluid and solid skeleton (so-called Skepton effect). However, it will be shown that for this material, testing at various loading rates

indicates that the strain-stress curve will not be much influenced by potential pore pressure incurred during loading. After the desired system temperature is achieved and stabilized, the confining pressure and vertical load are increased to the targeted downhole pressure value, so the specimen is initially loaded isotropically, and then the deviatoric load is increased until the specimen fails. Following ASTM-D7012, the specimen is tested at a constant rate (3.3×10^{-6} m/sec) so that specimen fails in approximately 10 to 15 minutes. During the test, the load frame records the axial position of the top piston. These data are used to derive the axial strain (e_A) of the specimen. It is important to note that Batch1 samples were not cut and polished on the cylinder ends. Batch2 had received this sample preparation prior to testing for to allow analysis at earlier stages of the stress-strain graph without the effects of surface defects. In addition, a new loading cell was needed, and replacement occurred between Batch1 and Batch2. The testing results of Batch1 are still reported in this study but caution should be used when comparing the results to other testing groups.

CHAPTER IV

RESULTS

This chapter displays the results measured and collected in this research study. Microscopy techniques are firstly used to evaluate microscale characteristics of chemical composition and microstructure in graphene and cement used in this study. Macroscopic properties important to well cement performance such as petrophysical and mechanical properties are then evaluated.

4.1. CHEMISTRY and COMPOSITION

4.1.1. ENERGY DISPERSIVE X-RAY SPECTROSCOPY

Energy dispersive x-ray spectroscopy of graphene samples provided elemental analysis used to indicate the quality and carbon content of each. Black shows the highest carbon content of ~95% and carbon to oxygen ratio. Platinum grade indicates a comparable quality to the previous, with minimum counts of residual elements. Diamond is observed to have the lowest carbon to oxygen content, but still of quality graphene with 88% carbon content and low counts of residual elements.

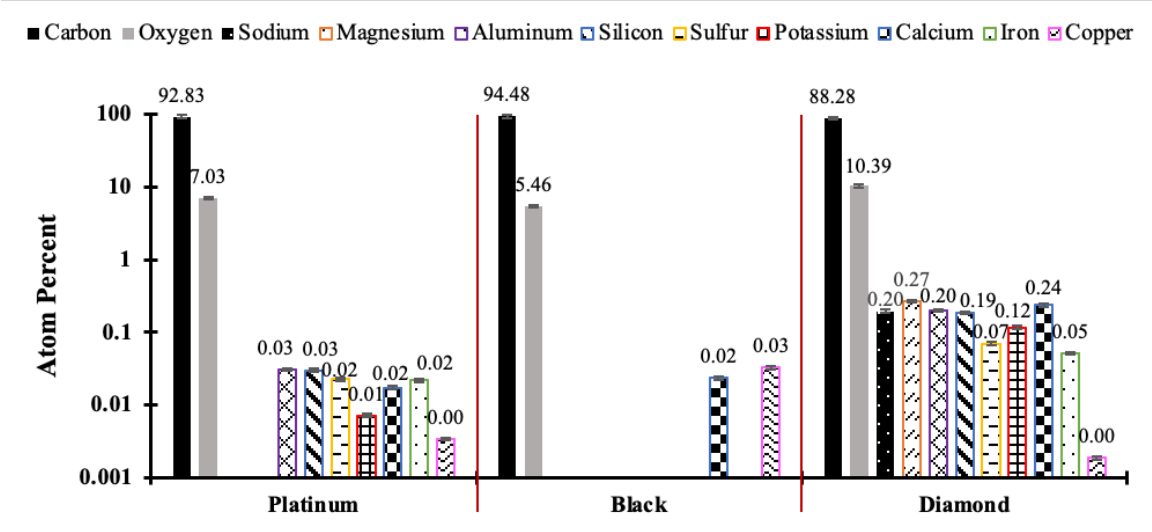

Figure 7 - The elemental compositions of three received graphene's were conducted to examine the EDS elemental compositions of each to be compared. Similar compositions are seen in Platinum and Black grade as both have carbon percentages of greater than 90% with minimal residual elements, while Diamond grade has a slightly lower carbon percentage while higher in oxygen and other elements.

Elemental mapping of the polished cement samples was taken to examine the composition of cement grains and matrix, along with observing any impact of GNPs on cement hydration chemistry. These two-dimensional maps of the cement surface were taken after indentation had occurred on the sample, to further characterize and correlate the micro-mechanical properties to chemistry. Figure 8 shows comparable elemental compositions and grain structures between neat and 0.05%GNPs hydrated cement. Some changes in high intensity silicon grains are observed in neat cement but are less apparent in the graphene cement. Very small but intense concentrations of carbon are observed only in graphene cement that could indicate grouping or clusters of GNPs within the matrix. In

order to be able to detect carbon phases, image and mapping acquisitions are done at a high magnification, due to the graphene nanoplatelet size and low percent dosage of GNP within the cement. EDS maps phase analysis was conducted in such regions at high magnification and observed the highlighted regions to have approximately 30% more carbon content than surrounding areas (Figure 9). These high carbon areas indicate graphene platelets clustered near fracture regions and the grain boundary of a partially hydrated cement clinker particle.

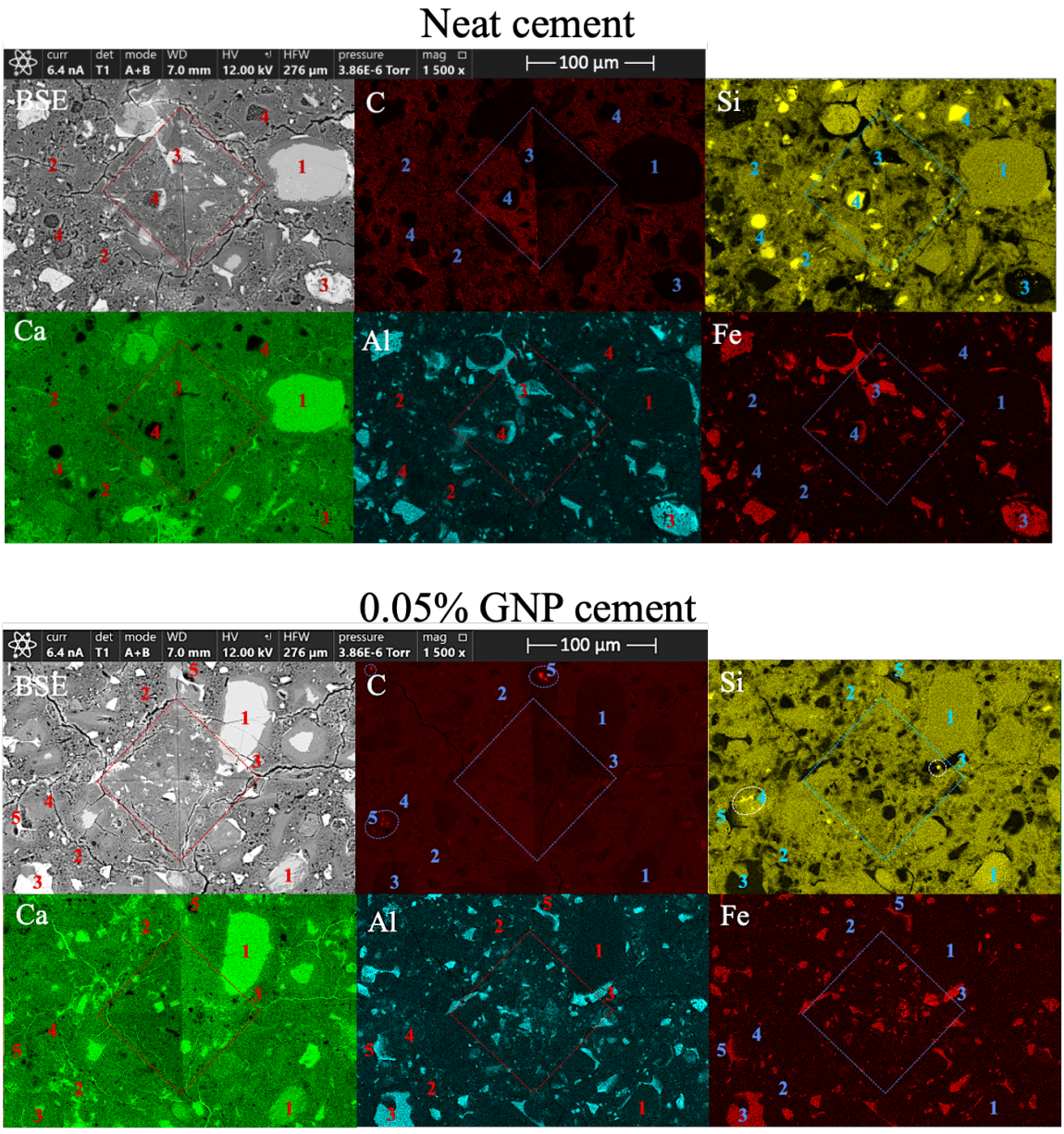

Figure 8 – Backscatter electron (BSE) image and EDS mapping of basic elements expected in cement of both polished neat and graphene cement samples. The dotted diamond shape shows the indentation made from the micro-Vicker's diamond tip, 1) Large unhydrated cement grains. 2) Low density calcium silicate hydrate (CSH) gel forms the matrix in-between grains. 3) Areas of high density consisting of primarily aluminum and iron. 4) Cement grains containing high concentration of mostly silicon. 5) Areas of relatively higher carbon content that could signify clustering of graphene nanoplatelets.

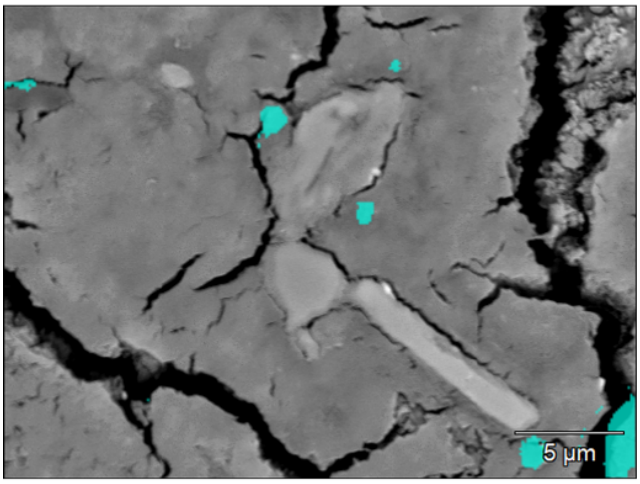

	GNP cement	
Element	Weight Percent	Atomic Percent
C	35.7	53.7
O	20.7	23.4
F	2.7	2.6
Mg	0.6	0.5
Al	0.9	0.6
Si	9.6	6.2
S	0.64	0.44
Ca	28.1	12.6
Fe	1.6	0.5

Figure 9 - EDS phase map in carbon rich hydrated cement highlighted regions near fracture regions and the grain boundary of a partially hydrated cement clinker particle, indicating possible graphene nanoplatelet clusters.

4.1.2. X-RAY FLOURECENSE

X-ray Fluorescence (XRF) was conducted on raw materials before cement mixing to analyze the chemical composition of cement powder and additional additives. As

expected, Class-H cement used in this study had large amounts of calcium and silicon oxides that are the basis of cement hydration.

Table 3 – Oxides present in the raw materials used for creating cement samples in this study.

Oxide Formula	Class-H cement	D-Air 5000	CFR-3	Bentonite
Al_2O_3	1.47	N/A	N/A	12.03
SiO_2	16.28	1.52	N/A	78.79
SO_3	6.97	61.47	98.81	N/A
K_2O	0.53	N/A	N/A	0.60
CaO	68.08	36.62	0.33	2.20
TiO_2	0.23	N/A	N/A	0.26
MnO	0.10	N/A	N/A	0.06
Fe_2O_3	5.93	N/A	N/A	5.72
ZnO	0.14	N/A	N/A	N/A
SrO	0.28	0.15	N/A	0.04
RhO	N/A	0.23	0.43	0.32
PdO	N/A	N/A	0.43	N/A

4.1.3. X-RAY DIFFRACTION

X-ray diffraction (XRD) was conducted to identify reacted hydration compounds and remaining unhydrated clinker in both neat and 0.1%GNP cement, the highest quantity graphene used in this study. 2-theta angle peaks are used to identify major phases within the hydrated cement and the CSH hump can be seen elevated from the baseline between 25° and 35° (Hunnicutt, 2013; Stutzman, 2011 ;Stutzman et al., 2016),

Little to no change in peaks or intensity in major cement compounds indicates that the addition of graphene does not chemically react or significantly affect the hydration process.

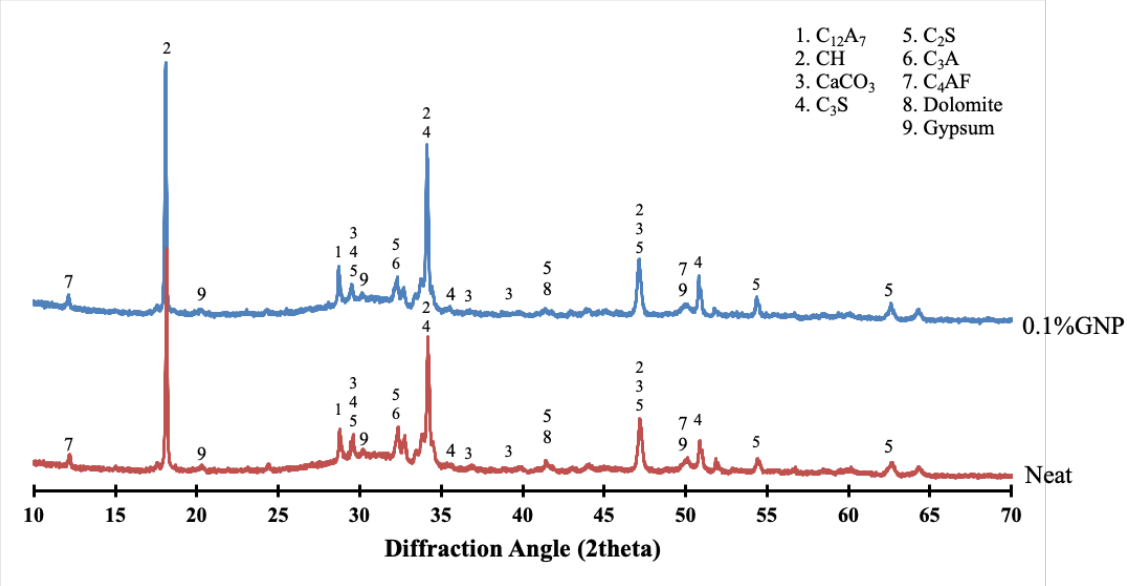

Figure 10 –Chemical composition is crushed and powdered hydrated cement using XRD to identify phases of hydration products and unhydrated remanence.

4.1.4. RAMAN SPECTROSCOPY

Spectrums obtained from Raman microscopy were used to evaluate the as-received GNP as well as graphene enhanced cement samples. The spectrum of GNPs in Figure 11shows the 3 peaks associated with graphene or graphene derivatives, D, G, and 2D at approximately 1350, 1580, and 2670 cm^{-1}, respectively (Wang et al., 2008). The low ratio of D-peak to G-peak counts indicate a low level of impurities are observed within the powder.

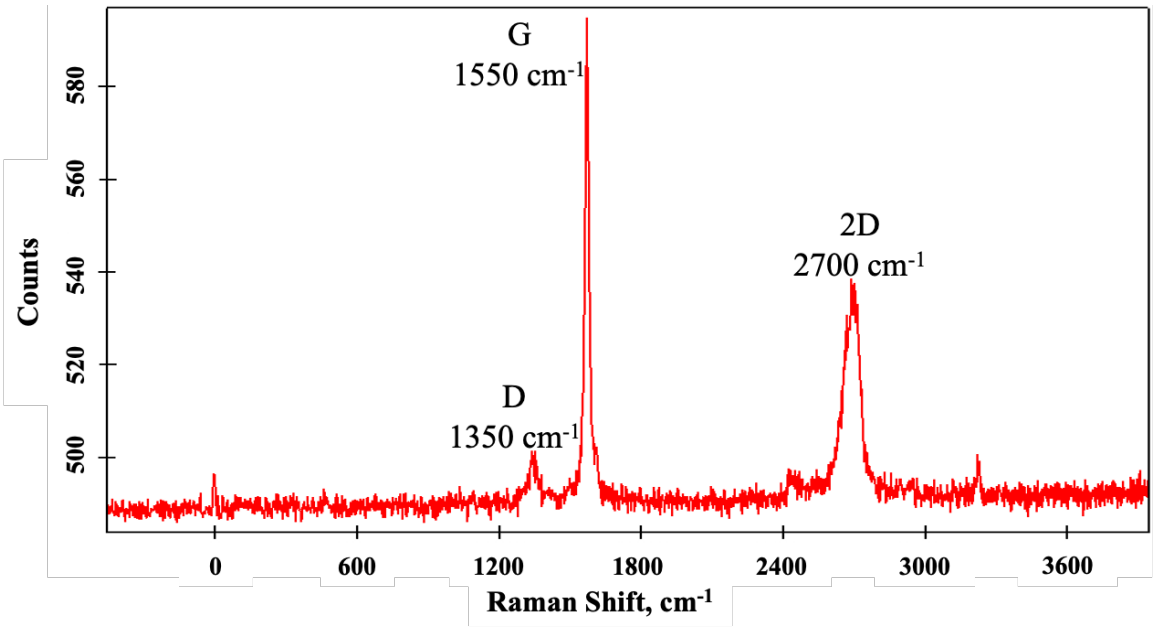

Figure 11 - Spectrum of graphene nanoplatelets before adding to cement. High G-peak in relation to D-peak indicates a high content of carbon chains with less impurities.

Spectrums were also gathered for neat and GNP cement polished samples for cement phases and profilometry of the sample surface (Figure 12). Raman shift approximate values for unhydrated cement phases are observed at 850cm^{-1} for tricalcium silicate (C_3S) and 1350cm^{-1} for tricalcium aluminate (C_3A), while hydrated phases are observed at 970-1100cm^{-1} for amorphous silica/calcium silicate hydrate (CSH), 1200cm^{-1} for gypsum, and 1570cm^{-1} for calcium hydroxide (CH) (Yarwood et al., 2009; Dunant et al., 2020). Spot spectrums were taken on cement clinker grains and the gel matrix to observe potential changes in chemical compounds during hydration.

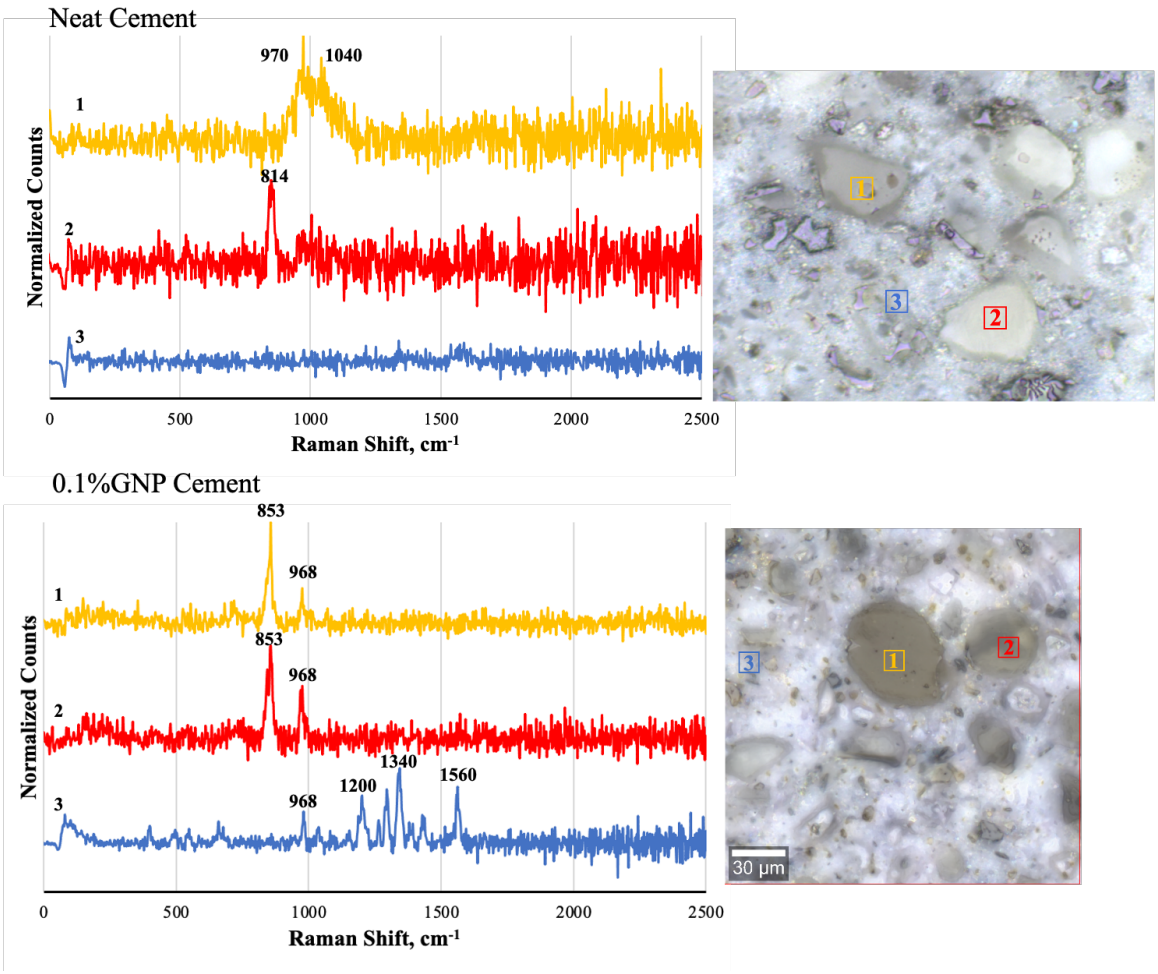

Figure 12 - Raman normalized spectrums of GNP cement A) point spectrums of three areas in the cement matrix. A1 spectrum of large cement clinker grain primarily of C3S at 853cm^{-1}. A2 indicates a smaller clinker grain with higher amorphous silica content at 968cm^{-1}. A3 spot of some matrix gel and small grains shows mixture of silica along with gypsum, C3A, and Ca(OH)2 at 1200, 1340, and 1560cm^{-1} respectively. B) Optical microscope image at 20x magnification with indicated spectrum spots. C) Surface profilometry of the polished sample shows elevated clinker grains indicated by lighter regions, and lower matrix and pores shown by darker colors.

4.2. MICROSTRUCTURE

4.2.1. TRANSMISSION ELECTRON MICROSCOPY

Transmission electron microscope (TEM) reveals the presence of multi-layered platelet stacking as observed. The smooth edges represent one atom thick graphene. The inserted arrows point to the boundaries between the different layers while the light regions indicate the less dense material where a greater number of electrons beam are transmitted, and darker areas are denser. The resolution of TEM is suitable to identify how individual platelets are arranged, and it provides a foundation for a larger field of view imaging using SEM.

Figure 13 - Graphene Platinum as received was onto a mesh grid for TEM imaging. (Left) Multiple layers of nanosheets are stacked across each other by indication of the defined lines in every direction. Possible folding of sheets indicated by the arrow shown. (Right) Clean edge of an orderly thin layering of sheets with edges going in the same direction.

4.2.2. SCANNING ELECTRON MICROSCOPY

From scanning electron microscopy (SEM) analysis, the three graphene grades were observed to view the morphology and microstructure. Platinum is observed to be composed of thin individual platelets that can be seen layered together and the multilayer platelets cluster together has layers with identifiable boundaries. Both Black and Diamond samples were observed to have few graphene platelets structures, but majorly composed of amorphous carbon structures. Platinum was the graphene chosen for use in this study due to its thin nanoplatelet structures and high carbon content, both of which were the desired properties and can be observed in other literature studies.

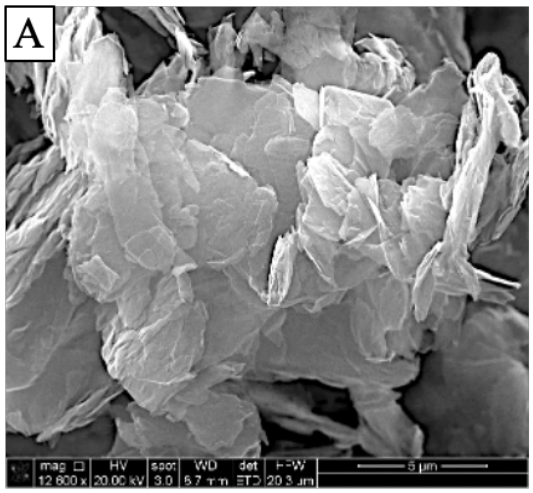

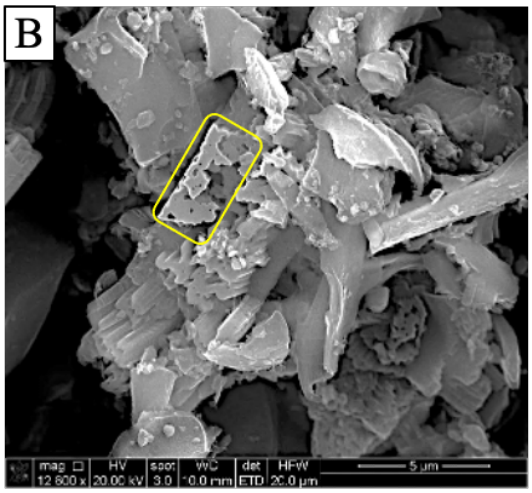

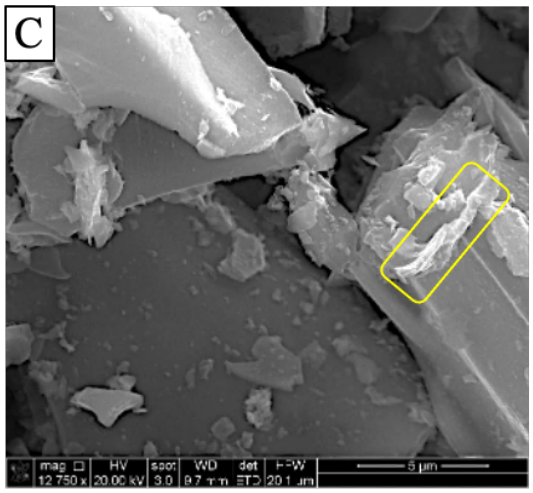

Graphene Type	Carbon Content (%)	Oxygen Content (%)
A) Platinum	92.8	7.0
B) Black	94.5	5.5
C) Diamond	88.3	10.4

Figure 14 - Graphene as received in 3 different types, each different in quality and form. Secondary electron SEM and EDS show each type of structure and atomic composition. A) Platinum is high grade graphene composed of approximately 93% carbon and 7% oxygen in the form of thin nanoplatelets layered together. B) Black is also high grade composed of 94% carbon and 5% oxygen with some platelets but mostly irregular shape and some possible biomaterial remnants. C) Diamond is a lower grade graphene composed of approximately 88% carbon, 10% oxygen, and less than 1% of other elements such as sodium, magnesium, aluminum, silicon,

calcium, etc. This type also takes the form of mostly irregular shapes with few platelets.

SEM of GNP enhanced Portland cement polished surfaces are seen to have graphene in pore spaces and crevices. The platelets appear to aggregate to these spaces and protrude from the pore walls. The clusters of platelets appear to be broken up into mono or multi-layered platelets during the slurry mixing or hydration process. Figure 15, all show graphene in different pore spaces, occupying a variety of volumes and displaying a different degree of aggregation/morphologies. shows a fractured surface of graphene enhanced cement sample which confirms GNP preference for pores and crevices, as observed in polished samples.

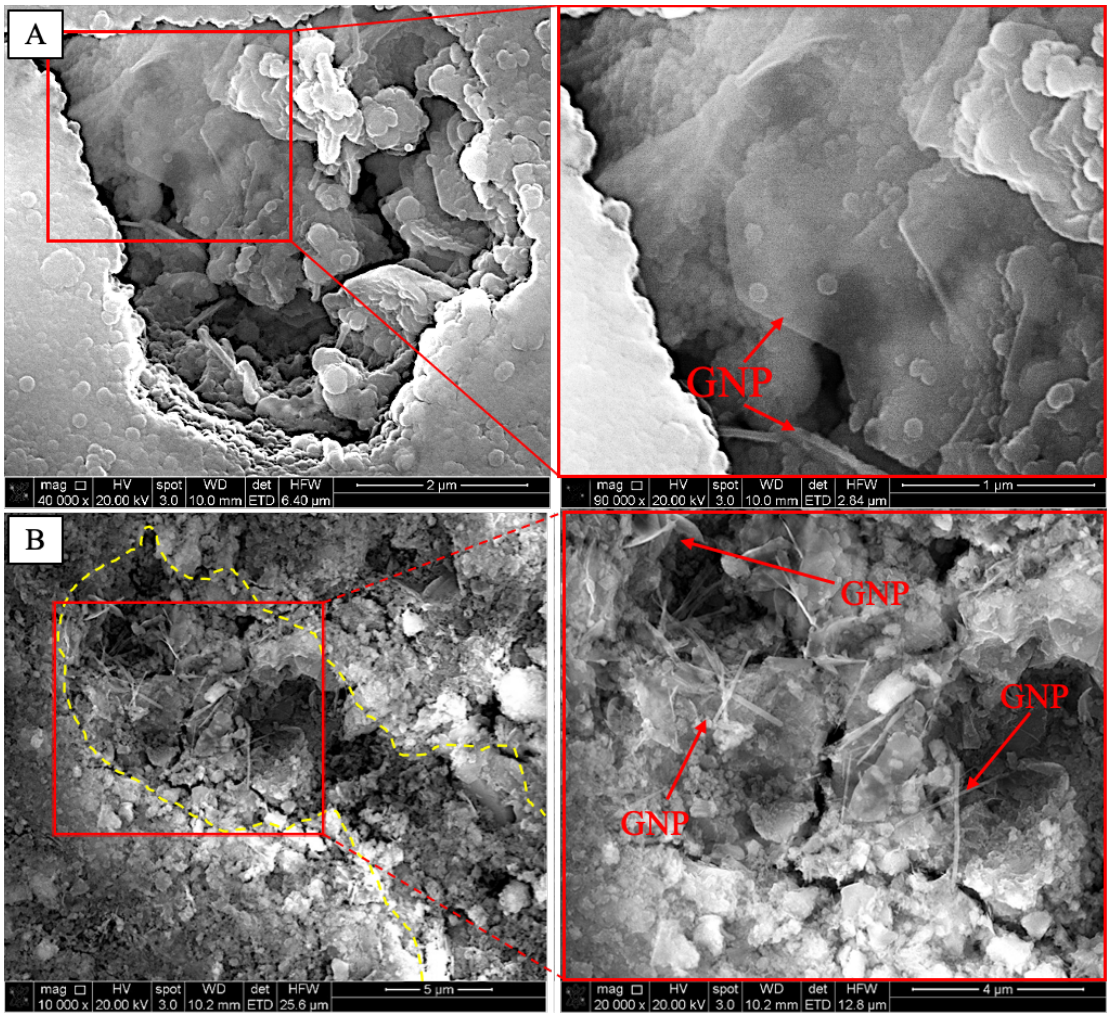

Figure 15 - SEM secondary electron images of graphene nanoplatelets on A) polished surface of graphene enhanced cement where platelets can be seen as thin and nearly transparent protruding out from the pore wall into open pore spaces B) fractured surface where clusters and grouping of graphene platelets are seen within a crevice.

4.2.3. COMPUTED TOMOGRAPHY SCANNING

Computed tomography (CT) scanning was conducted on post failure samples after triaxial testing to view how the failure occurred and what fracture patterns are observed.

Cylinders were removed from confinement and placed into an industrial CT scanner. Neat cement has a dense fracture network that propagates down through more than half the sample length. 0.05% and 0.1%GNPs exhibit less void space and fracture networks after failure (Figure 16). This toughness and resistance to fracturing are important to prevent permeability and fluid leakage even after mechanical failure. In sample Batch2, the same behavior was observed (Figure 17) with as little as 0.008% graphene addition to the cement. Total failure of the neat cement sample had resulted in the separation of fractured pieces when removed from confinement and CT scan of neat in Figure 17 would not be representative of the fracture thickness at simulated condition. Regardless, the addition of graphene improved the resistance to fracturing and separation, that would be beneficial to maintain zonal isolation after the failure of the cement plug.

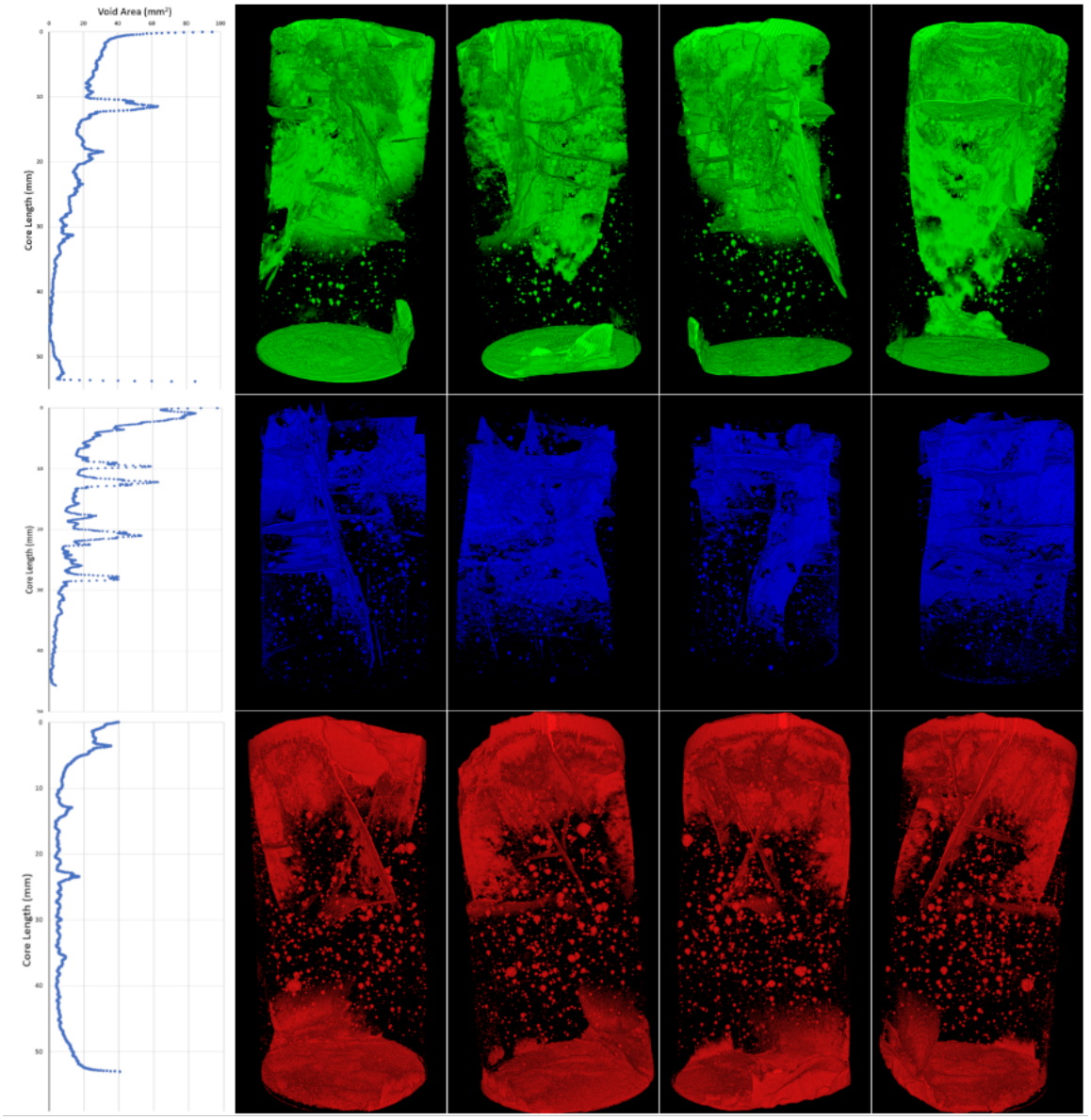

Figure 16 – Three-dimensional CT scan rendering of cement cylinders after confined compression testing showing fracture networks within the samples of neat (Top), 0.05%GNPs (Middle), and 0.1%GNPs (Bottom).

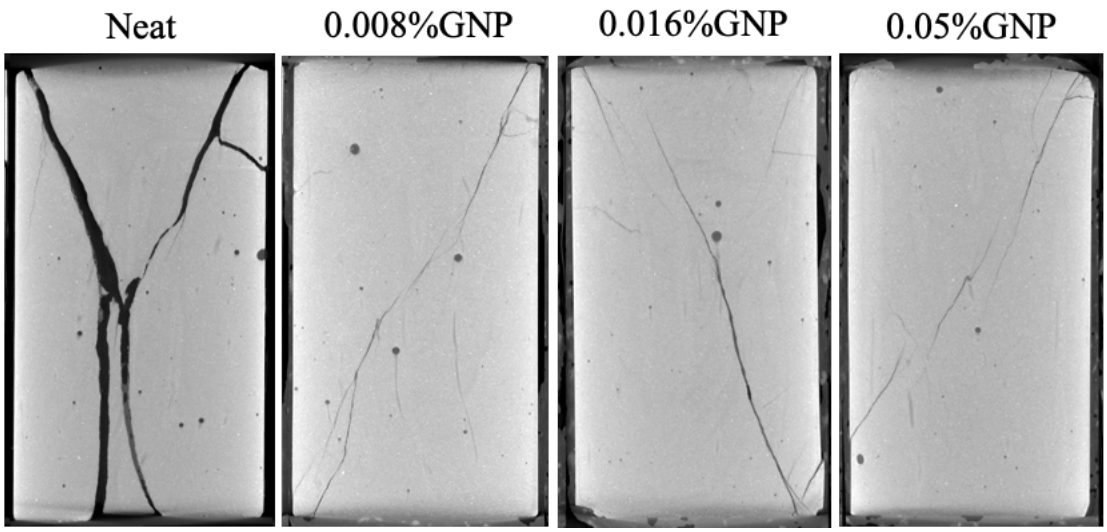

Figure 17 - CT scanning slice of post triaxial mechanical testing illustrating the fracture pattern of the failed samples. A reduced fracture network and conductivity is observed at failure when graphene is added.

4.3. PETROPHYSICS

4.3.1. POROSITY and GAS PERMEABILITY

Porosity and permeability measurements were taken to compare any potential changes in the cement petrophysical properties due to graphene nanoplatelets addition. Porosity, measured with helium gas and mercury injection showed no significant change along with pore throat distribution when graphene was added. Permeability measurements using the helium gas and simulated confining pressure of 13.7 MPa (2,000psi) show small variations in the gas permeability of less than 10 micro-Darcy's when graphene is added to the cement (Figure 18).

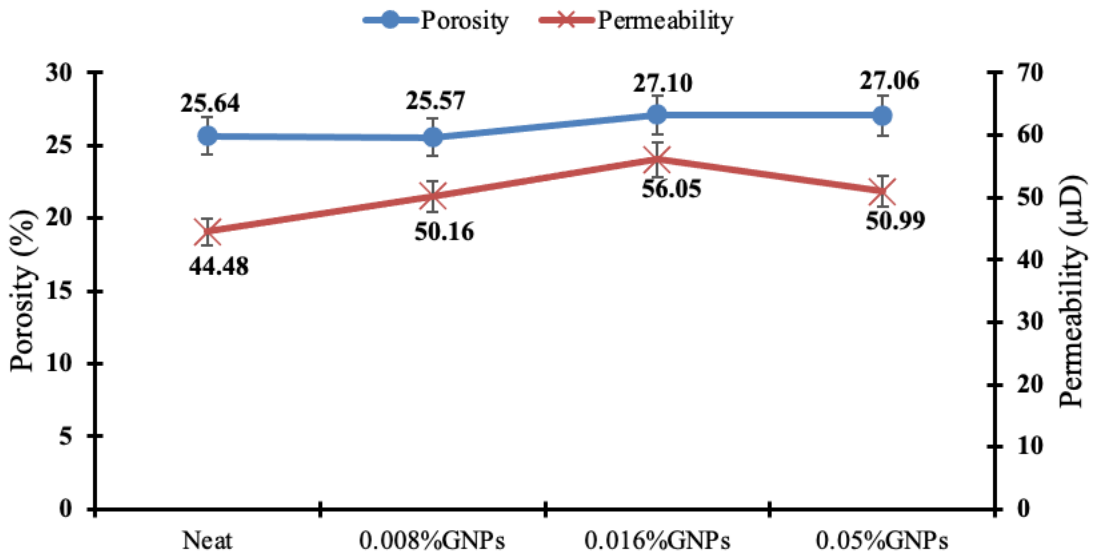

Figure 18 – Helium gas porosity and permeability measurements obtained for samples neat, 0.008%, 0.016%, and 0.05%GNPs cement. Permeability tested at simulated confining pressure of 13.7 MPa (2,000psi).

4.3.2. PORE STRUCTURE

Petrophysical properties were also evaluated using MIP with the increasing pressure gradually forced the mercury to intrude into the sample pore spaces and the amount of mercury injected, expressed as a fraction of the sample pore volume. Addition of graphene had not significantly altered the porosity, 1% increase, and pore throat radii, 5% reduction (Figure 19). In Figure 20, a higher frequency of 0.025µm pore is observed in 0.05%GNP as opposed to greater frequency of other pore throat sizes, such as 0.075 along with 0.0075 and smaller, in the nano range seen in neat cement.

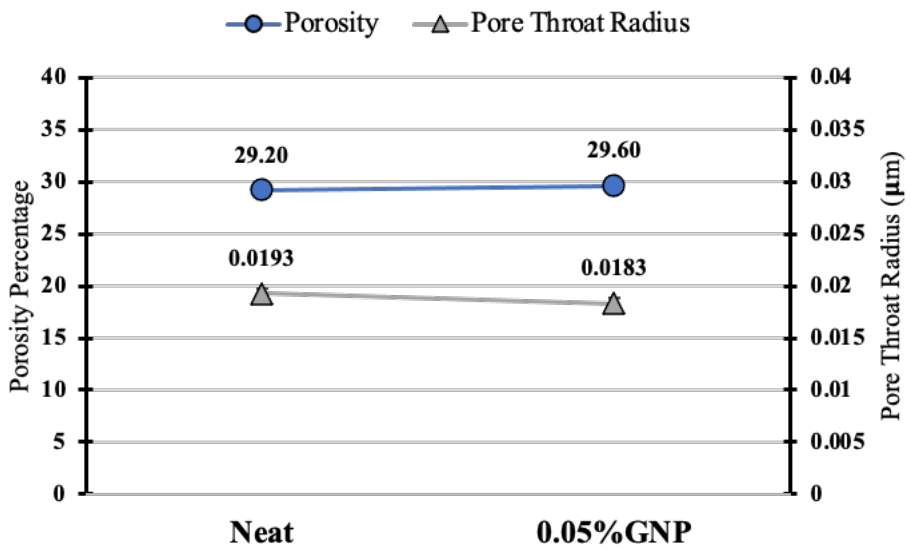

Figure 19 - Porosity and median pore throat radius obtained through MIP of cement samples.

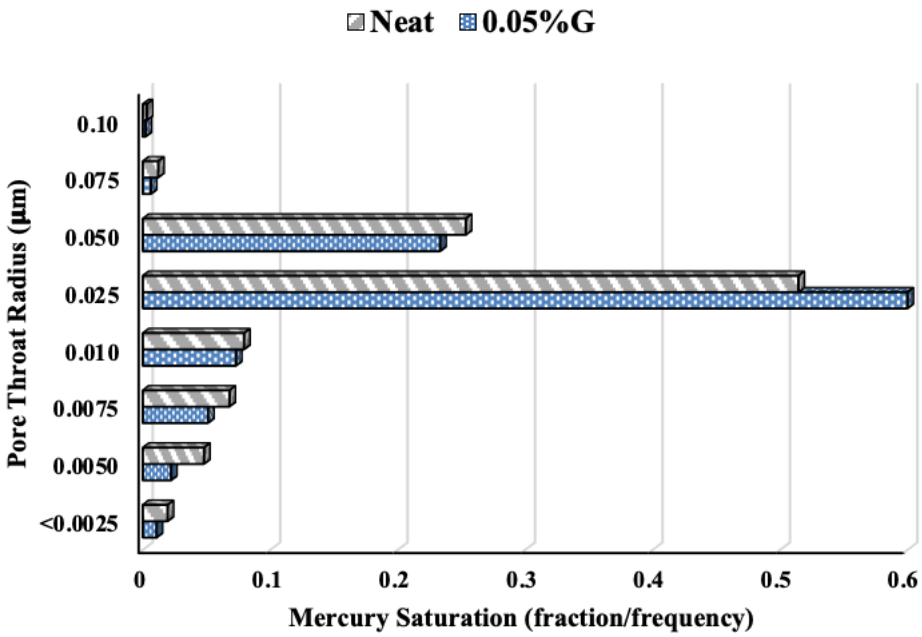

Figure 20 - A narrower pore size distribution around 0.025µm is seen in 0.05%GNP cement when compared to neat cement that has a higher frequency of 0.075 and <0.010 pore throats.

4.4. MECHANICAL PROPERTIES

4.4.1. INDENTATION

The Young's modulus and microhardness for hydrated samples of neat cement and GNP cement were calculated for each indent using ASTM E2546 using the loading and unloading and averaged for the respective sample. Table 4 shows a reduced average rebound Young's modulus in the microstructure with graphene added to the cement at 0.008% but no significant change in other concentrations compared to neat cement. The hardness of the cement is shown to be reduced by approximately 15% in the lower two graphene concentrations but neat and 0.05%GNP are observed to have approximately the same hardness values.

Table 4 – Summary of micro-indentation results of elasticity and hardness of cement microstructure.

	Neat	0.008%GNP	0.016%GNP	0.05%GNP
Elastic Modulus	11.95 GPa	8.74 GPa	13.22 GPa	11.67 GPa
Hardness	0.33 GPa	0.27 GPa	0.27 GPa	0.32 GPa

SEM was taken of indentations made on both Neat and 0.05%GNP polished samples. High magnification images show fractures propagate through some indentation sites while others propagate around the perimeter, and Vicker's diamond imprints measure approximately 120-160 microns in diameter (Figure 21).

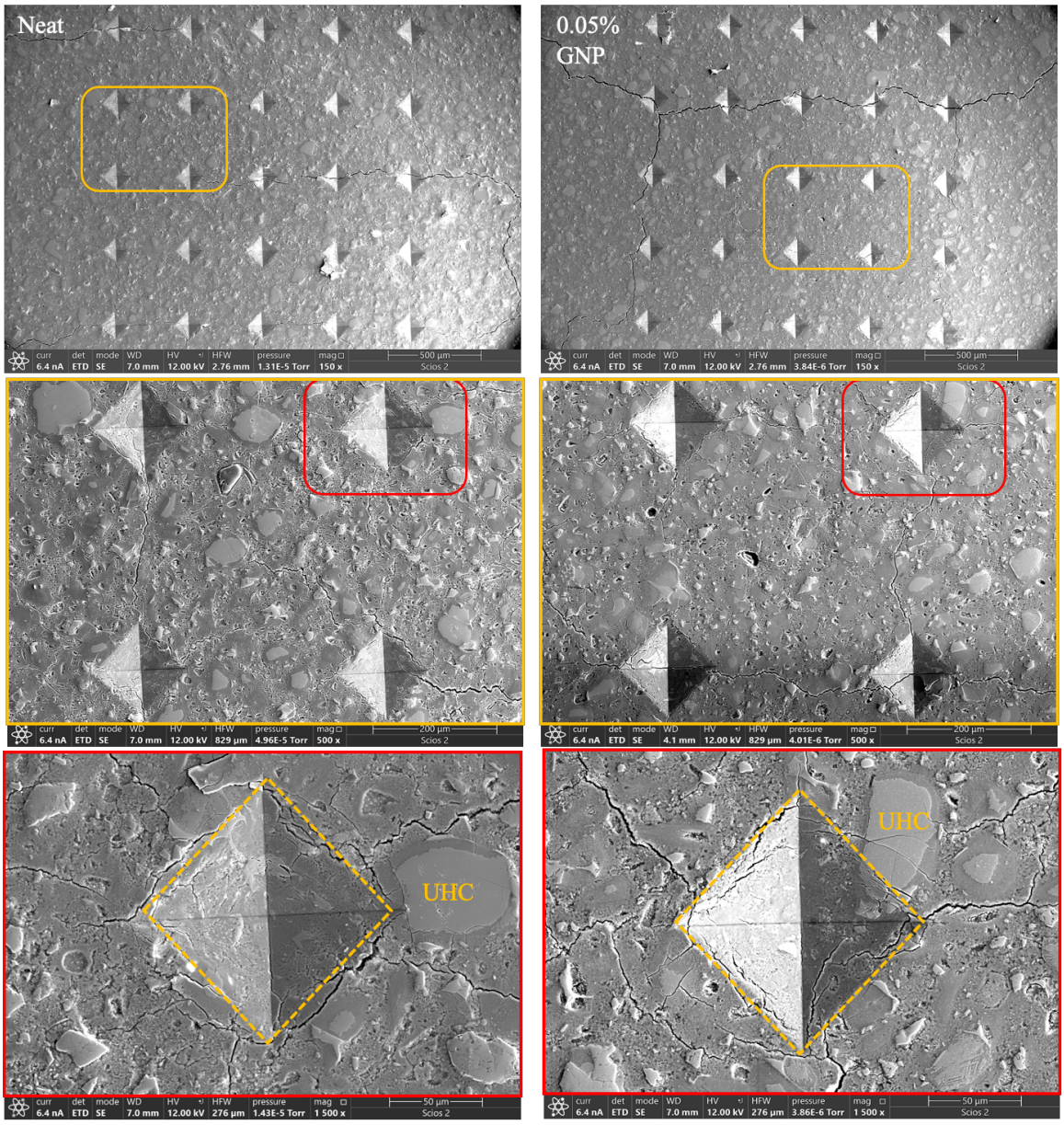

Figure 21 - Secondary electron SEM images of indentation matrix made in polished (Left) neat and (Right) 0.05%GNPs samples. Low to high magnification images show global indentation matrix to single indent marks where some relatively large unhydrated or partially hydrated cement grains (UHC) within the matrix and the local fracture network tracing the indentation outline.

4.4.2. TRIAXIAL LOAD TESTING

In this study triaxial load testing is conducted to evaluate the cement mechanical performance with the addition of GNPs at simulating reservoir conditions for its application, specifically when the testing conditions are 13.7-41.3 MPa confining pressure and 90℃ temperatures. For Batch1 at a confining pressure of 41.3 MPa, the maximum axial stress of 0.05%GNPs is 14.3% and is 22.7% for 0.1%GNPs greater compared to neat cement. At a confining pressure of 13.7 MPa, the maximum axial stress of 0.008%GNP is 15.56%, 0.016%GNP is 17.23%, and for 0.05%bwoc is 25.04% greater compared to neat cement. Graphene overall enhances the strength of the cement when tested at simulating downhole conditions of pressure and temperature. The strain values at failure for each sample are 0.0083, 0.0119, 0.0108, and 0.0112 for neat, 0.008%, 0.016%, and 0.05%GNPs, respectfully.

Also, Young's modulus of neat cement obtained from triaxial testing is maintained between 13.6 to 16.0 GPa (Batch2) when tested at these simulated conditions. However, a higher modulus value of 6.38% and 13.64% than the control (neat) is observed for 0.016% and 0.05% graphene addition, respectively. The lowest percentage of GNPs addition, 0.008%, showed the lowest Young's modulus with a value of 13.6 GPa, indicating a higher compliance.

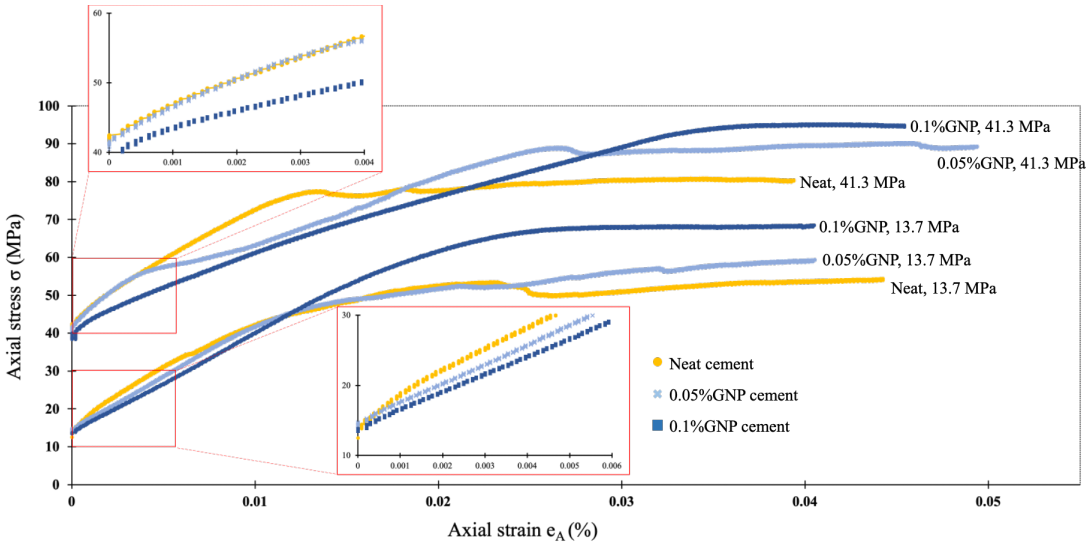

Figure 22 - Strain-stress curve of Batch1 neat cement, 0.05%bwoc graphene cement, and 0.1%bwoc graphene cement tested at 13.7 and 41.3 MPa and 90°C. The initial linear regime is shown in a magnified scale in the inset and the slope of this initial linear regime is used to calculate the Young's Modulus.

Table 5 – Summary of average Batch1 sample triaxial testing results

	Neat cement		**0.05% GNP- cement**		**0.1% GNP- cement**	
	Ultimate Axial Strength	Young's modulus	Ultimate Axial Strength	Young's modulus	Ultimate Axial Strength	Young's modulus
Confining pressure at 13.7 MPa	53.5 MPa	3.4 GPa	59.5 MPa	2.9 GPa	68.3 MPa	2.5 GPa
Percentage change at 13.7 MPa			**11.2%**	**14.7%**	**27.7%**	**26.5%**
Confining pressure at 41.3 MPa	77.5 MPa	3.2 GPa	88.6 MPa	3.2 GPa	95.1MPa	2.1 GPa
Percentage change at 41.3 MPa			**14.3%**	**0.0%**	**22.7%**	**34.4%**

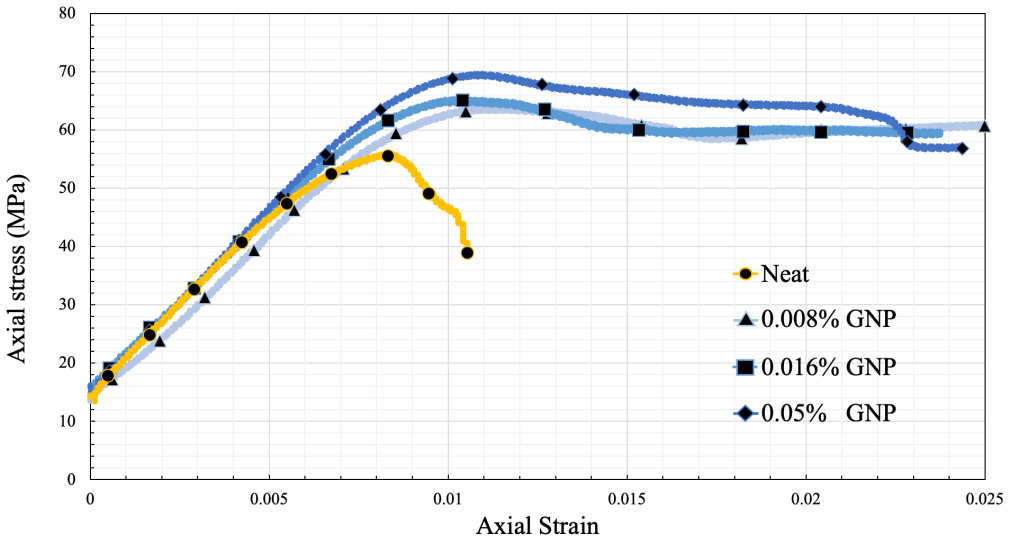

Figure 23 - Strain-stress curve of Batch2 neat cement, 0.008%, 0.016%, and 0.05%GNP cement tested at 13.7 MPa and 90°C. The initial linear regime is shown in a magnified scale in the inset and the slope of this initial linear regime is used to calculate the Young's Modulus.

Table 6 – Summary of average Batch2 sample triaxial testing results

	Neat		**0.008%GNP**		**0.016%GNP**		**0.05%GNP**	
	Ultimate Axial Strength	Young's modulus	Ultimate Axial Strength	Young's modulus	Ultimate Axial Strength	Young's modulus	Ultimate Axial Strength	Young's modulus
Confining pressure at 13.7 MPa	55.72 MPa	14.1 GPa	64.39 MPa	13.6 GPa	65.32 MPa	15.0 GPa	69.67 MPa	16.0 GPa
Percentage change at 13.7 MPa	Control group	Control group	**15.56 %**	**-3.83 %**	**17.23 %**	**6.38 %**	**25.04 %**	**13.64 %**

CHAPTER V

DISCUSSION, CONCLUSION AND FUTURE WORK

5.1. DISCUSSION

Based on the evidence of microstructural and chemical composition results, the graphene nanoplatelets addition to wellbore cement had shown little to no significant impact on cement hydration for slurry designs and curing conditions tested in this study. A potential explanation for this is the low percentage of graphene added (between 0 and 0.1%), the chemically unreactive nature of GNPs in highly alkaline cement pore water, and its hydrophobic nature. However, improvements in mechanical properties of hydrated Portland cement GNPs added in small amounts could be explained by the occupation of the GNPs in micro pore and fracture walls indicating that the weakest or failing points of the cement has mechanical reinforcement by the strongest material.

As per graphene oxide platelets reported in several publications, atypical hydration product crystals were obtained in SEM images with shapes similar to that of a “lotus-flower” by Lv et al. (2014). The atypical shape of these crystals, when compared to typical cement hydration products, growing on the graphene platelets, with a lower length to width aspect ratio than CSH needles, could be a potential reason for the improvement in the strength of the cement. Dunant et al. (2020) have demonstrated that the length to width of CSH crystal structures correlate with Young’s Modulus as longer-thinner crystals, such

as needles, have a higher modulus and a more brittle nature whereas the lattice like structures would behave in a more ductile manner. The formation of these atypical crystal morphologies of cement hydration products and their aspect ratio as reported by Lv et al. (2014) and Dunant et al. (2020), is a plausible explanation for a triaxial test higher shear strength for graphene cement compared to neat cement under the same testing conditions. This study provides evidence that the shear strength increases with an increase in the percentage of graphene when samples are tested at reservoir like conditions. Specifically, as shown in Figure 23, when the testing conditions are 13.7 MPa confining pressure and 90℃, the maximum axial stress of 0.008%GNP is 15.56%, 0.016%GNP is 17.23%, and for 0.05%bwoc is 25.04% greater compared to neat cement. Compare mechanical results to that seen in literature, Qureshi and Panesar (2020) conducted a study of the effects of GO, rGO, and graphene on cement properties when added to Portland cement. Mechanical tests for compressive and flexural strength had been conducted on various percentages of the three graphene-based materials. After 28 days of hydration, they viewed that the graphene composite had the greatest increase in compressive strength, 39% at 0.02%bwoc compared to neat, with rGO and GO increasing the compressive strength by 30% at 0.04%bwoc and 28% at 0.04%bwoc, respectively. Furthermore, all their mechanical testing of both compressive and flexural strength testing for the three additives showed an increase in strength compared to neat Portland cement when hydrated at 14 and 28 days. Although they are different mechanical tests, an increase in cement shear strength observed in our study when graphene is added to cement is in agreement with published data which suggest improved mechanical properties due to the addition of GNP. While simulating downhole-like conditions, triaxial loading tests at

relevant T are the most relevant, and in this study, resistance to stress of cement samples had increased by 15%-26% with the addition of 0.008, 0.016, 0.05, and 0.1%GNPs (Figure 22 and Figure 23).

Similarly, to the triaxial load tests, the micro-indentation of 0.008%GNP resulted in the lowest Young's modulus with a decrease of 26.86% compared to neat cement. Further comparing to the control sample, 0.016%GNP shows an increased microstructure modulus by 10.63% but no significant reduction in 0.05%GNP (Table 4). Even though the moduli from triaxial testing and micro indentation have different values due to confinement/lack thereof, similar elastic behavior is observed when graphene is added to the cement. Also, Young's modulus of the wellbore cement obtained from triaxial testing is maintained between 13.6 to 16.0 GPa when tested at these simulated conditions. However, a higher modulus value of 6.38% and 13.64% than the control (neat) is observed for 0.016% and 0.05% graphene addition, respectively. The lowest percentage of GNP addition, 0.008%, showed the lowest Young's modulus with a value of 13.6 GPa, indicating a higher compliance. It is worth noting that most cement strength testing reported in published studies is achieved by unconfined compression or flexural strength tests, which are following the API standards. However, these testing standards are no longer fit into the situation where high temperature and high pressure are prevailing at in-situ conditions. Thus, in this study, strength testing is at wellbore conditions of pressure, temperature, and confining stress. As such, Young's modulus values obtained from triaxial testing (Table 6) are falling into the ranges which are previously reported as 13.1 GPa by Katende et al. (2020). As well, Al-Rub et al. (2012) observed an elastic modulus of 13-15 MPa from flexural strength testing of carbon nanotubes cement composites. This

differentiation can be due to the cement's water saturation and its effects during triaxial loading (Macecot et al., 2019).

Furthermore, the addition of graphene nanoplatelets to Portland cement-based slurry significantly changes the strain-stress behavior in the triaxial load test and provides much more ductility. For example, as summarized in Figure 23, when the 0.05%GNP reached its peak axial stress at the testing conditions of 13.7 MPa confining pressure and 90°C, the corresponding strain is 0.0048. However, when the neat cement reached its peak strength under the same testing conditions, the corresponding strain is 0.0034, resulting in lower strength and deformation. More importantly, in all cases of graphene addition to cement, significant ductile deformation followed the peak stress, and the duration of the ductile stage lasted until the end of the test. However, in neat cement, peak stress was briefly followed by an abrupt stress drop of a 10-15 MPa, which marks the end of a brief ductile deformation and progression to permanent deformation and the ultimate failure. This indicates that there is a reduced brittle behavior prior to the failure of the graphene cement. With the increased mechanical properties of wellbore cement seen in this study, it is possible to assume that the addition of graphene nanoplatelets would maintain or improve cement strength while reducing the amount of cement used. This is important as cement is mass produced and used all over the world, generating large CO_2 emissions and the implementation of more efficient use of ordinary Portland cement is needed (UN Environment, 2018). Even more importantly, enhanced ductility of wellbore cements, either in primary wellbore construction or in plugging and abandonment of wellbores, would prolong durability and prevent leakage due to failure under increased pressure.

The more brittle-like strain stress behavior of neat cement was also captured by the macroscopic fracture patterns observed after the mechanical testing at conditions of 13.7 MPa confining pressure and 90°C using CT scanning. Figure 16 shows a rotating montage of 3-dimensional reconstruction of slices imaged through each cement: (Top) Neat cement, (Middle) 0.05%bwoc, and (Bottom) 0.1%bwoc graphene cement. As shown in Figure 16 (Top), a network of fractures formed and propagated through the whole neat cement specimen with a complete failure of the cement core by significant fracturing at the top of the sample. Fewer fractures were observed in 0.05%bwoc graphene cement, with more distributed propagation of the fractures, Figure 16 (Middle). However, as shown in Figure 16 (Bottom), the fracture network is still tightly connected with fewer void spaces in the 0.1% graphene cement and the fewest fractures were observed, with fractures primarily propagating from the periphery of the cylinder. Similar results are seen when the amount of graphene is reduced to 0.008%GNPs and no apparent total failure of the cement sample (Figure 17). The length and width of this fracture are relatively small when compared with the fracture observed on the neat cement, which means its propagation was arrested during the test and that fewer fracture propagations with increased graphene content resulted in an increased ductility and resistance to fracture initiation and reduced fracture propagation, which is also observed in the axial stress-strain data.

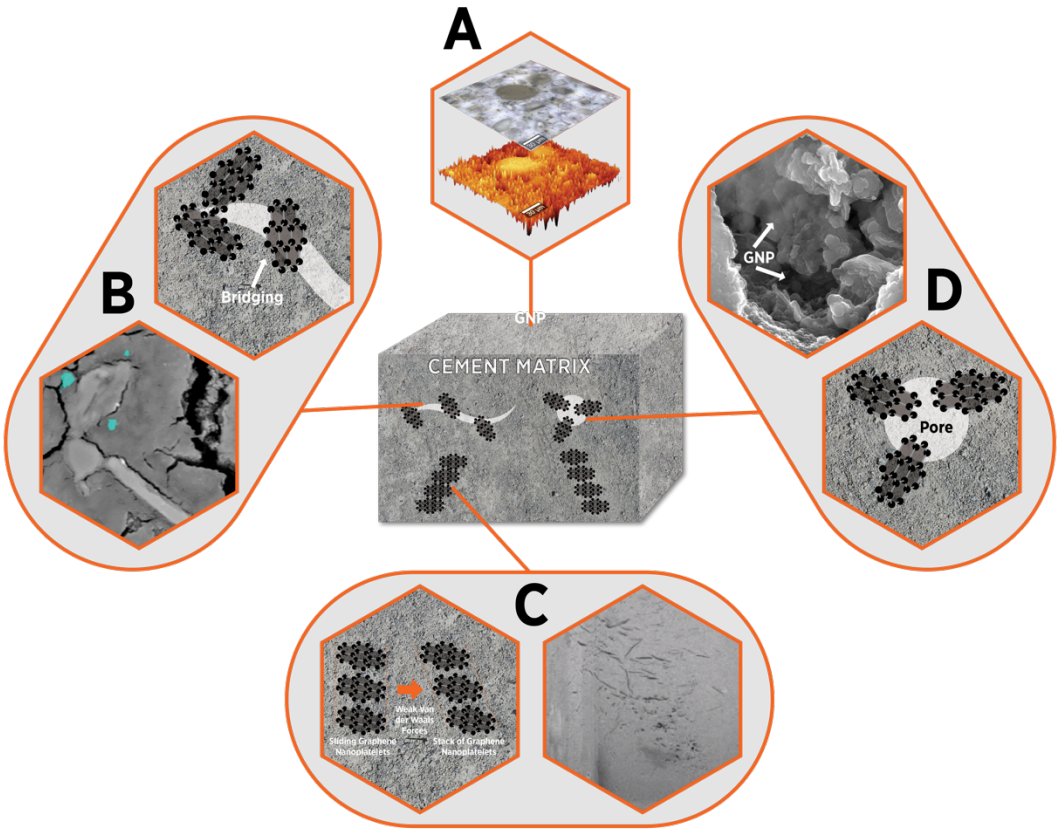

Figure 24 - A) Profilometry of polished cement surface show larger clinker grains raised above the darker CSH gel matrix. B) Looking below the surface, graphene nanoplatelets (GNPs) within the cement matrix tend to bridge fractures and inhibit fracture propagation. C) Schematic interpretation of potential mechanism how graphene platelets slide under load within the CSH, resembling a deck of cards, resulting in reinforcing the matrix and ductile behavior due to the relatively weak Van der Waals forces between the platelets. D) Graphene lines the pore walls within the cement. These three mechanisms result in ductile behavior and reduction of fracturing, rather than the typical brittle nature of hydrated Portland cement paste when subject to loading. Images not to scale in order to achieve clarity of mechanism, GNP is drawn much larger than in reality.

Potential mechanism of how graphene enhances ductility and reduces Young's modulus in cement. "Graphene is a material that brings out the best in every other material that it is added to" (personal communication, G. King) and does so with the addition of very minimal amounts of <1%. The mechanism by which this is accomplished is not completely resolved. As earlier stated, some of it is driven by the strategic positioning of very strong GNP in micropores, as well as a potential change of CSH morphology, which leads to an increased Youngs modulus. However, the transition from brittle to a more ductile nature of cement in the triaxial loading test is the most likely result of the GNP sliding like a deck of cards within the cement matrix, and has been seen in other matrices as well (Alexopoulos et al., 2017). This is similar to the mechanism of lubrication in which stacked layers of graphene are attached by weak Vander Waals forces and can easily slide over one another. Berman et al. (2014) in a review on graphene as an emerging lubricant demonstrated lubrication depends on stacking, structural features, and the nature of the sliding surfaces. In our samples, we observed thin layers of graphene stacked together under TEM (Figure 13). SEM images of graphene cement (Figure 15) indicate that most of the graphene is distributed within the pore spaces or weakest parts of the material, which facilitate fracture initiation and propagation during loading. An increase in the ductility and axial strength of graphene cement (Figure 23) could result from the sliding of graphene in the weak areas as opposed to breakage in the neat cement upon loading. The higher strain values observed in graphene cement compared to neat further supports this sliding mechanism. Graphene also renders the material less brittle as seen by a decrease in Young's modulus with 0.008%GNP but no alteration to hardness observed from micro-indentation hardness analysis (Table 4). Wang et al. (2020) have shown that 5% rGO added to ceramics

bridges fractures and undergoes folding after unloading a tensile load and unfolding during reloading and is a unique deformation property of multi-layer graphene material. The study also showed that toughening of the rGO material occurs at cracks where thick rGO is pulled out represents a 200% improvement in fracture toughness over reference Al_2O_3 ceramic. The modification of Young's modulus, ultimate axial stress, and increased strain are depicted by the conceptual model shown in Figure 24. Graphene occupies the pores spaces in the cement matrix, Figure 24D, reinforcing the pore structures, the strongest material adds strength to the weakest point in cement. The graphene layers are held by weak Vander Waals forces (Figure 24C) which are easily displaced when the sample is loaded. Upon loading, the cement properties are modified as described above. When the cement begins to fail and fracturing occurs, graphene platelets block the propagation of fractures (Figure 24B) and prevents the formation of a large fracture network and total failure of the cement.

5.2. CONCLUSIONS

The addition of graphene nanoplatelets to a Class-H wellbore cement slurry increases the ultimate axial stress by up to 25% under triaxial loading with just 0.05%bwoc added. Furthermore, the addition of GNP decreases Young's modulus 3 to 26 percent with 0.008%bwoc added and therefore reduces the stiffness of the hydrated cement. Hence GNP creates the most desirable combination of increased strength and increased flexibility in wellbore cement. This combination will enable improved cement performance and its mechanical failure because the higher strength increases resistance to breakage and the reduction of brittle failure decreases the tendency for large stresses

to develop as the cement is subjected to drivers such as the casing and/or surrounding rock expanding and contracting due to temperature and pressure changes.

Providing further support to the observation of GNP additive improving the resistance of cement to failure, in the triaxial tests at reservoir-relevant temperature and pressures used in this study of 90°C and 13.7MPa, the cement with GNP additive exhibits the ability to sustain larger strain at failure. The GNP-cement also does not exhibit brittle failure observed in neat cement, as the strain at failure increases from 30.1 to 43.3% when graphene is added, with strain failure values of 0.0083, 0.0119, 0.0108, and 0.0112 for neat, 0.008%, 0.016%, and 0.05%GNPs, respectfully. As well, a sharp drop in axial stress was observed in neat cement after failure whereas GNP cement had held stress for a prolonged strain period. Indeed, post-testing CT scans show development of a pronounced set of fractures for the neat cement with void areas reaching ~65 mm^2 in the densely fractured region. The presence of distinct fractures is reduced to a maximum of ~35mm^2 in the case of 0.1% graphene addition.

Besides impacts on strength and flexibility, the addition of GNPs additive exhibited little to no effect on cement porosity and permeability as results with the addition of graphene are within range of the neat cement.

While ongoing efforts are required to more fully grasp both the chemical and physical mechanism(s) by which GNP impact wellbore cement properties, the potential for improving performance is clearly shown. Additionally, while it remains to understand and quantify impacts of other details of cement chemistry, including contamination by drilling fluid during cement placement, the clear impact is possible even with additive rations as low as 0.008%bwoc to 0.05%bwoc. Finally, microstructural analysis

systematically observing GNP placement in the pore structure as a function of physio-chemical conditions during hydration is necessary to better connect GNP-cement chemistry, microstructure, and macroscopic properties. However, the present work makes clear for a hypothesis that GNPs migrate to discontinuities within the cement matrix during hydration, such as pore throats and fractures, resulting in increased strength and higher flexibility, all of which drive wellbore cement technology toward greater cement resistance to failure from physical loading.

5.3. FUTURE WORK

There is a high potential in the future pairing of graphene nanoplatelets and cementitious material that can build off this and other research studies. One such future is the need for cement service life over 10,000 years as a recent stress test on graphene shows, not only is this material comparable to Earths core in terms of pressure/stress it can withstand (100 GPa), but more importantly, it demonstrates that the monolayer of graphene can endure a fatigue life of 10^9 cycles at mean stress of 71 GPa (Cui et al 2020). Aiding in cement fatigue life could possibly provide a one-and-done long lasting plug capable of withstanding the underground cyclic pressures and temperature seen in many current wellbores.

Another addition to this study is the possibility for simulating full reservoir conditions directly after it is mixed. Using an environmental chamber of pressure, temperature, and humidity could provide information on the potential difference in the role that graphene may take at during hydration at HTHPs within the wellbore, whether it be chemical, physical, or thermal.

REFERENCES

Aasnes, M. Ø. (2017). Evaluation of Methods and Quality Barriers in Plug and Abandonment-Technology Advances, Physical and Governing Requirements. NTNU,

Achang, M., Yanyao, L., & Radonjic, M. (2020). A Review of Past, Present, and Future Technologies for Permanent Plugging and Abandonment of Wellbores and Restoration of Subsurface Geologic Barriers. Environmental Engineering Science.

Alexopoulos, N. D., Paragkamian, Z., Poulin, P., & Kourkoulis, S. K. (2017). Fracture related mechanical properties of low and high graphene reinforcement of epoxy nanocomposites. Composites Science and Technology, 150, 194-204.

Al-Rub, R. K. A., Ashour, A. I., & Tyson, B. M. (2012). On the aspect ratio effect of multi-walled carbon nanotube reinforcements on the mechanical properties of cementitious nanocomposites. Construction and Building Materials, 35, 647-655.

Allison, E., and Mandeler, B. (2019). Abandoned wells. Petroleum and the Environment, American Geosciences Institute, part 7/24.

Alvarez, R. A., Zavala-Araiza, D., Lyon, D. R., Allen, D. T., Barkley, Z. R., Brandt, A. R., Davis, K. J., Herndon, S. C., Jacob, D. J., & Karion, A. (2018). Assessment of methane emissions from the US oil and gas supply chain. science, 361(6398), 186-188.

API Standard RP 10B, Recommended Practice for Testing Well Cements, 22nd. Washington, DC: API, 2.

ASTM. (2007). Standard Practice for Instrumented Indentation Testing. Designation: E2546-07, ASTM International.

ASTM. (2010). Standard Test Method for Compressive Strength and Elastic Moduli of Intact Rock Core Specimens Under Varying States of Stress and Temperatures: ASTM International.

ASTM. (2014). Standard Test Method for Static Modulus of Elasticity and Poisson's Ratio of Concrete in Compression (ASTM C469/C469M-14).

Baomin, W., & Shuang, D. (2019). Effect and mechanism of graphene nanoplatelets on hydration reaction, mechanical properties and microstructure of cement composites. Construction and Building Materials, 228, 116720.

Barnes, P., & Bensted, J. (2002). Structure and performance of cements. CRC Press.

Bello, K. S. (2014). Experimental Assessment of Cement Integrity under Thermal Cycle Loading Conditions in Geopressured Geothermal Reservoirs.

Bensted, J., & Barnes, P. (2008). The structure and properties of cement. Chemical industry, Beijing.

Berg, S., Kutra, D., Kroeger, T., Straehle, C. N., Kausler, B. X., Haubold, C., Schiegg, M., Ales, J., Beier, T., Rudy, M., & Eren, K. (2019). Ilastik: interactive machine learning for (bio) image analysis. Nature methods, 16(12), 1226-1232.

Berman, D., Erdemir, A., & Sumant, A. V. (2014). Graphene: a new emerging lubricant. Materials today, 17(1), 31-42.

Boehm, H., Setton, R., & Stumpp, E. (1985). Nomenclature and terminology of graphite intercalation compounds. Report by a subgroup of the international committee for characterization and terminology of carbon and graphite on suggestions for rules for the nomenclature and terminology of graphite intercalation compounds. Synthetic metals, 11(6), 363-371.

Bogaerts, M., Kanahuati, A., Khalilova, P., Moretti, F., Voon, E., & Dighe, S. (2012, June). Challenges in setting cement plugs in deep-water operations. In SPE Deepwater Drilling and Completions Conference. OnePetro.

Bois, A. P., Garnier, A., Rodot, F., Saint-Marc, J., & Aimard, N. (2011). How to prevent loss of zonal isolation through a comprehensive analysis of microannulus formation. SPE Drilling & Completion, 26(01), 13-31.

Botas, C., Álvarez, P., Blanco, C., Gutiérrez, M. D., Ares, P., Zamani, R., . . . Menéndez, R. (2012). Tailored graphene materials by chemical reduction of graphene oxides of different atomic structure. *RSC advances, 2*(25), 9643-9650.

Brown, R., Shukla, A., & Natarajan, K. R. (2002). Fiber reinforcement of concrete structures.

Brufatto, C., Cochran, J., Conn, L., Power, D., El-Zeghaty, S. Z. A. A., Fraboulet, B., Griffin, T., James, S., Munk, T., Justus, F., & Rishmani, L. (2003). From mud to cement—building gas wells. Oilfield Review, 15(3), 62-76.

Chemistry and Quality Control Formulas in the Cement Industry. (2020, June 07). Retrieved November, 2021, from https://thecementinstitute.com/chemistry-and-quality-control-formulas-in-the-cement-industry/.

Chen, Z., Zhou, F., & Rahman, S. S. (2014). Effect of cap rock thickness and permeability on geological storage of CO2: laboratory test and numerical simulation. Energy exploration & exploitation, 32(6), 943-964.

Cui, T., Mukherjee, S., Sudeep, P. M., Colas, G., Najafi, F., Tam, J., Ajayan, P.M., Singh, C.V., Sun, Y., & Filleter, T. (2020). Fatigue of graphene. Nature materials, 19(4), 405-411.

Downey, M. W. (1984). Evaluating seals for hydrocarbon accumulations. AAPG bulletin, 68(11), 1752-1763.

Dreyer, D. R., Ruoff, R. S., & Bielawski, C. W. (2010). From conception to realization: an historical account of graphene and some perspectives for its future. Angewandte Chemie International Edition, 49(49), 9336-9344.

Du, H., Radonjic, M., & Chen, Y. (2020). Microstructure and micro-geomechanics evaluation of Pottsville and Marcellus shales. Journal of Petroleum Science and Engineering, 195, 107876.

Dunant, C. F., Granja, J., Muller, A., Azenha, M., & Scrivener, K. L. (2020). Microstructural simulation and measurement of elastic modulus evolution of hydrating cement pastes. Cement and Concrete Research, 130, 106007.

Fink, J. (2012). Petroleum engineer's guide to oil field chemicals and fluids. Gulf Professional Publishing.

Fischer-Cripps, A. C. (2007). Introduction to contact mechanics (Vol. 101): Springer.

Frazier, Z. (2020, September 21). Plugging abandoned oil wells is one 'green new deal' aspect loved by both Republicans and Democrats. OklahomaMinerals.com. Retrieved November 17, 2021, from https://www.oklahomaminerals.com/plugging-abandoned-oil-wells-is-one-green-new-deal-aspect-loved-by-both-republicans-and-democrats.

Gadgil, B., Damlin, P., & Kvarnström, C. (2016). Graphene vs. reduced graphene oxide: A comparative study of graphene-based nanoplatforms on electrochromic switching kinetics. Carbon, 96, 377-381.

Gardner, T. and Reuters. (2021). “Bipartisan Senate Bill Would Direct Billions to Plugging Wells.” Hart Energy, 14 Apr. 2021, 10:01 AM, www.hartenergy.com/news/bipartisan-senate-bill-would-direct-billions-plugging-wells-193525.

Goral, J., Panja, P., Deo, M., Andrew, M., Linden, S., Schwarz, J. O., & Wiegmann, A. (2020). Confinement effect on porosity and permeability of shales. Scientific reports, 10(1), 1-11.

Gorchov Negron, A. M., Kort, E. A., Conley, S. A., & Smith, M. L. (2020). Airborne Assessment of Methane Emissions from Offshore Platforms in the US Gulf of Mexico. Environmental science & technology, 54(8), 5112-5120.

Groom, N. (2020). Special report: millions of abandoned oil wells are leaking methane, a climate menace, Reuters.

Han, M., Muhammad, Y., Wei, Y., Zhu, Z., Huang, J., & Li, J. (2021). A review on the development and application of graphene based materials for the fabrication of modified asphalt and cement. Construction and Building Materials, 285, 122885.

Horst, D. J., Duvoisin, C. A., & de Almeida Vieira, R. (2018). An Overview on Properties, Production Mechanisms and Applications of Graphene. Int. J. of Eng. Trends and Technology, 61(3), 156-160.

Hunnicutt, W. (2013). Characterization of calcium-silicate-hydrate and calcium-alumino-silicate-hydrate.

Kaiser, M. J. (2015). Decommissioning forecast in the deepwater Gulf of Mexico, 2013–2033. Marine Structures, 41, 96-126.

Katende, A., Lu, Y., Bunger, A., & Radonjic, M. (2020). Experimental Quantification of The Effect Of Oil Based Drilling Fluid Contamination On Properties Of Wellbore Cement. Journal of Natural Gas Science and Engineering, 103328.

King, G.E., and King, D.E. (2013). Environmental risk arising from well-construction failure—Differences between barrier and well failure, and estimates of failure frequency across common well types, locations, and well Age. SPE Prod. Oper. 28, 323.

Kong, W., Kum, H., Bae, S.-H., Shim, J., Kim, H., Kong, L., Meng, Y., Wang, K., Kim, C., Kim, J. (2019). Path towards graphene commercialization from lab to market. Nature nanotechnology, 14(10), 927-938.

Lecampion, B., Bunger, A., Kear, J., & Quesada, D. (2013). Interface debonding driven by fluid injection in a cased and cemented wellbore: Modeling and experiments. International Journal of Greenhouse Gas Control, 18, 208-223.

Lee, C., Wei, X., Kysar, J. W., & Hone, J. (2008). Measurement of the elastic properties and intrinsic strength of monolayer graphene. science, 321(5887), 385-388.

Liu, Y., Ma, T., Wu, H., & Chen, P. (2020). Investigation on mechanical behaviors of shale cap rock for geological energy storage by linking macroscopic to mesoscopic failures. Journal of Energy Storage, 29, 101326.

Liversidge, D., Taoutaou, S., & Agarwal, S. (2006, September). Permanent plug and abandonment solution for the North Sea. In SPE Asia Pacific Oil & Gas Conference and Exhibition. OnePetro.

Lv, S., Liu, J., Sun, T., Ma, Y., & Zhou, Q. (2014). Effect of GO nanosheets on shapes of cement hydration crystals and their formation process. Construction and Building Materials, 64, 231-239.

Lv, S., Ma, Y., Qiu, C., Sun, T., Liu, J., & Zhou, Q. (2013). Effect of graphene oxide nanosheets of microstructure and mechanical properties of cement composites. Construction and Building Materials, 49, 121-127.

Malecot, Y., Zingg, L., Briffaut, M., & Baroth, J. (2019). Influence of free water on concrete triaxial behavior: The effect of porosity. Cement and Concrete Research, 120, 207-216.

McNaught, A. D., & Wilkinson, A. (1997). Compendium of chemical terminology (Vol. 1669): Blackwell Science Oxford.

Mehta, P. K., Monteiro, P. J., & Concrete-Microstructure, P. (2006). Materials. McGrawHill, PJM, United States, 85-86.

Mokhtar, M., Abo-El-Enein, S., Hassaan, M., Morsy, M., & Khalil, M. (2017). Mechanical performance, pore structure and micro-structural characteristics of graphene oxide nano platelets reinforced cement. Construction and Building Materials, 138, 333-339.

Moraes, W., De Bruijn, G. G., Fagundes, L., Sobreira, M., Silvestri, R., & Moretti, F. (2013, October). Successful Cement Plug in HPHT Pre-Salt Offshore Well in Brazil. In OTC Brasil. OnePetro.

Na, S., Sun, W., Ingraham, M. D., & Yoon, H. (2017). Effects of spatial heterogeneity and material anisotropy on the fracture pattern and macroscopic effective toughness of Mancos Shale in Brazilian tests. Journal of Geophysical Research: Solid Earth, 122(8), 6202-6230.

Nelson, E. B., & Guillot, D. (2006). Well cementing. Sugar Land, Tex.: Schlumberger.

Neuberger, N., Adidharma, H., & Fan, M. (2018). Graphene: A review of applications in the petroleum industry. Journal of Petroleum Science and Engineering, 167, 152-159.

Neville, A. M., & Brooks, J. J. (1987). Concrete technology (pp. 8-40). England: Longman Scientific & Technical.

North, J., Brangetto, M. P., & Gray, E. (2000, February). Central Graben Extreme Offshore High-Pressure/High-Temperature Cementing Case Study. In IADC/SPE Drilling Conference. OnePetro.

O'Kane, M. "Final report of the independent review of coal seam gas activities in NSW." NSW Government, Sydney, Australia 16 (2014).

Olabode, A., & Radonjic, M. (2013). Experimental investigations of caprock integrity in CO2 sequestration. Energy Procedia, 37, 5014-5025.

Olabode, A., & Radonjic, M. (2014). Shale caprock/acidic brine interaction in underground CO2 storage. Journal of Energy Resources Technology, 136(4).

Oliver, W. C., & Pharr, G. M. (1992). An improved technique for determining hardness and elastic modulus using load and displacement sensing indentation experiments. Journal of materials research, 7(6), 1564-1583.

Olutimehin, A. A., & Odunuga, M. (2012, February). A model to minimize risk of cement plug failure in HPHT conditions. In North Africa Technical Conference and Exhibition. OnePetro.

Pakulski, M., Qu, Q., & Pearcy, R. (2005, February). Gulf of Mexico deepwater well completion with hydrate inhibitors. In SPE International Symposium on Oilfield Chemistry. OnePetro.

Pan, Z., He, L., Qiu, L., Korayem, A. H., Li, G., Zhu, J. W., . . . Wang, M. C. (2015). Mechanical properties and microstructure of a graphene oxide–cement composite. Cement and Concrete Composites, 58, 140-147.

Petty, S., Gastineau, J., Bour, D. L., & Ravi, K. (2003). Life Cycle Modeling of Wellbore Cement Systems Used for Enhanced Geothermal System Development. Paper presented at the 28th Workshop on Geothermal Reservoir Engineering, Stanford U.(27–29 January 2003).

Qureshi, T. S., & Panesar, D. K. (2020). Nano reinforced cement paste composite with functionalized graphene and pristine graphene nanoplatelets. Composites Part B: Engineering, 108063.

Rahman, M. J., Fawad, M., & Mondol, N. H. (2020). Organic-rich shale caprock properties of potential CO2 storage sites in the northern North Sea, offshore Norway. Marine and Petroleum Geology, 122, 104665.

Rios, R., & Ars, F. (2021, August). Plug and Abandonment Materials-Technology Landscape. In Offshore Technology Conference. OnePetro.

Rusch, D. W. (2004, October). Subsea Leaks Cured with pressure-activated sealant. In SPE Asia Pacific Oil and Gas Conference and Exhibition. OnePetro.

Schindelin, J., Arganda-Carreras, I., Frise, E., Kaynig, V., Longair, M., Pietzsch, T., Preibisch, S., Rueden, C., Saalfeld, S., & Schmid, B. (2012). Fiji: an open-source platform for biological-image analysis. Nature methods, 9(7), 676-682.

Schowalter, T. T. (1979). Mechanics of secondary hydrocarbon migration and entrapment. AAPG bulletin, 63(5), 723-760.

Sobolev, K., Flores, I., Hermosillo, R., & Torres-Martínez, L. M. (2006). Nanomaterials and nanotechnology for high-performance cement composites. Proceedings of ACI session on nanotechnology of concrete: recent developments and future perspectives, 91-118.

Sone, H. (2012). Mechanical properties of shale gas reservoir rocks, and its relation to the in-situ stress variation observed in shale gas reservoirs. Stanford University.

Stutzman, P. (2011). Direct determination of phases in 68ortland cements by quantitative X-ray powder diffraction. NIST Technical note, 1692, 59.

Stutzman, P. E., Feng, P., & Bullard, J. W. (2016). Phase analysis of Portland cement by combined quantitative X-ray powder diffraction and scanning electron microscopy. Journal of research of the National Institute of Standards and Technology, 121, 47-107.

Tiwari, S. K., Sahoo, S., Wang, N., & Huczko, A. (2020). Graphene research and their outputs: Status and prospect. Journal of Science: Advanced Materials and Devices, 5(1), 10-29.

UN Environment, Scrivener, K. L., John, V. M., & Gartner, E. M. (2018). Eco-efficient cements: Potential economically viable solutions for a low-CO2 cement-based materials industry. Cement and Concrete Research, 114, 2-26.

Vavra, C. L., Kaldi, J. G., & Sneider, R. M. (1992). Geological applications of capillary pressure: a review. AAPG bulletin, 76(6), 840-850.

Vrålstad, T., Saasen, A., Fjær, E., Øia, T., Ytrehus, J. D., & Khalifeh, M. (2019). Plug & abandonment of offshore wells: Ensuring long-term well integrity and cost-efficiency. Journal of Petroleum Science and Engineering, 173, 478-491.

Wang, Q., Ramírez, C., Watts, C. S., Borrero-López, O., Ortiz, A. L., Sheldon, B. W., & Padture, N. P. (2020). Fracture, fatigue, and sliding-wear behavior of nanocomposites of alumina and reduced graphene-oxide. Acta Materialia, 186, 29-39.

Warne, P. (2004). Decommissioning-north sea. Oil, Gas & Energy Law, 2(2).

Wisen, J., Chesnaux, R., Werring, J., Wendling, G., Baudron, P., & Barbecot, F. (2020). A portrait of wellbore leakage in northeastern British Columbia, Canada. Proceedings of the National Academy of Sciences, 117(2), 913-922.

Yang, H., Cui, H., Tang, W., Li, Z., Han, N., & Xing, F. (2017). A critical review on research progress of graphene/cement based composites. Composites Part A: Applied Science and Manufacturing, 102, 273-296.

Zeng, Y., Liu, R., Li, X., Zhou, S., Tao, Q., & Lu, P. (2019). Cement sheath sealing integrity evaluation under cyclic loading using large-scale sealing evaluation equipment for complex subsurface settings. Journal of Petroleum Science and Engineering, 176, 811-820.

Zhao, Z., Qi, T., Zhou, W., Hui, D., Xiao, C., Qi, J., Zheng, Z., & Zhao, Z. (2020). A review on the properties, reinforcing effects, and commercialization of nanomaterials for cement-based materials. Nanotechnology Reviews, 9(1), 303-322.

Zhu, W., & Bartos, P. J. (2000). Application of depth-sensing microindentation testing to study of interfacial transition zone in reinforced concrete. Cement and Concrete Research, 30(8), 1299-1304.

Zhu, Y., Murali, S., Cai, W., Li, X., Suk, J. W., Potts, J. R., & Ruoff, R. S. (2010). Graphene and graphene oxide: synthesis, properties, and applications. Advanced materials, 22(35), 3906-392.

VITA

Cody Massion

Candidate for the Degree of

Master of Science

Thesis: CHARACTERIZATION OF GRAPHENE NANO PLATELETS REINFORCED WELLBORE CEMENT

Major Field: Petroleum Engineering

Biographical:

Education:

Completed the requirements for the Master of Science in your major at Oklahoma State University, Stillwater, Oklahoma in December 2021.

Completed the requirements for the Bachelor of Science in Mechanical Engineering at Oklahoma State University, Stillwater, Oklahoma in 2015.

Presentations and Publications:

Massion, C., Achang, M., Bour, D., & Radonjic, M. (2020). Graphene-enhanced wellbore cement: improving cement performance in the construction of geothermal wellbores. Accepted and presented at GRC2020 conference. GRC Transactions, Volume 44, 67-81.
Massion, C., Lu, Y., Bunger, A., Crandall, D., & Radonjic, M. (2021). Impact of Graphene and the Testing Conditions on the Wellbore Cement Mechanical and Microstructural Properties. https://onepetro.org/ARMAUSRMS/proceedings-abstract/ARMA21/All-ARMA21/ARMA-2021-2089/468345.
Massion, C., Lu, Y., Bunger, A., Crandall, D., & Radonjic, M. (2021). Improvement of Wellbore Cement by Addition of Graphene Nanoplatelets. Accepted and presented at GRC2021 conference. GRC Transactions, Volume 45, #193.
Massion, C., Vissa, S. V. K., Lu, Y., Bunger, A., Crandall, D., & Radonjic, M. (2021). Geomimicry inspired MicroNano Concrete as Subsurface Hydraulic Barrier Materials: Learning from Shale Rocks as Best Geological Seals. Accepted and to be presented at TMS2022 Annual Meeting and Exhibition.